NOTICE

The quality of this microform is heavily dependent upon the quality of the original thesis submitted for microfilming. Every effort has been made to ensure the highest quality of reproduction possible.

If pages are missing, contact the university which granted the degree.

Some pages may have indistinct print especially if the original pages were typed with a poor typewriter ribbon or if the university sent us an inferior photocopy.

Previously copyrighted materials (journal articles, published tests, etc.) are not filmed.

Reproduction in full or in part of this microform is governed by the Canadian Copyright Act, R.S.C. 1970, c. C-30.

AVIS

La qualité de cette microforme dépend grandement de la qualité de la thèse soumise au microfilmage. Nous avons tout fait pour assurer une qualité supérieure de reproduction.

S'il manque des pages, veuillez communiquer avec l'université qui a conféré le grade.

La qualité d'impression de certaines pages peut laisser à désirer, surtout si les pages originales ont été dactylographiées à l'aide d'un ruban usé ou si l'université nous a fait parvenir une photocopie de qualité inférieure.

Les documents qui font déjà l'objet d'un droit d'auteur (articles de revue, tests publiés, etc.) ne sont pas microfilmés.

La reproduction, même partielle, de cette microforme est soumise à la Loi canadienne sur le droit d'auteur, SRC 1970, c. C-30.

Canada

Some Properties of the Semimagnetic Semiconductor Alloy System $Cd_{2x}(CuGa)_yMn_{2z}Te_2$

by

Roger D. Goudreault

Thesis submitted to the
School of Graduate Studies
in partial fulfillment of
the requirements for the degree of
Master of Science

Department of Physics
University of Ottawa
Ottawa, Ontario

October 30th, 1987

ISBN 0-315-46768-1

UNIVERSITÉ D'OTTAWA
UNIVERSITY OF OTTAWA

Abstract

Some forty polycrystalline samples of the $Cd_{2x}(CuGa)_yMn_{2z}Te_2$ (x+y+z=1) alloy system were prepared in order to investigate its crystallographic, optical and magnetic properties.

In the crystallographic analysis, Debye-Scherrer x-ray powder photographs were used i) to determine equilibrium conditions, ii) to determine lattice parameter values, and iii) to provide an approximate isothermal section of the alloy system; approximate because the samples near the chalcopyrite field did not achieve equilibrium.

Room-temperature measurements of optical absorption were made to give values of optical energy gap E_g for all single phase samples. It was found that discontinuities in the linear variation of E_g with composition were due to the formation of an 'ordered' zinc blende and an 'ordered' chalcopyrite phase field. The nature of this ordering however has not been determined.

Measurements of the electron spin resonance (ESR) were made as a function of temperature in the range 4.2 - 500 K on single phase samples. The curves of ESR linewidth, ΔH versus temperature were analysed in terms of a relation developed by Woolley et al. (87W2).

Measurements of low-field magnetic susceptibility in the temperature range 4.2 - 250 K were made to give values of T_g, the spin-glass transition temperature and θ, the Curie-Weiss temperature. Values of T_g and lattice parameter were analysed for the zinc blende samples in terms of the indirect superexchange mechanism of the form $J(r) = I_o\, r^{-2} \exp(-\alpha r)$ proposed by Geertsma et al. (77G1). From that analysis, the values of I_o and α obtained were found to agree with those obtained for similar zinc

blende alloys (87A1, 87M1, 87W2). Values of the Curie-Weiss θ for each sample were also calculated from the values of I_o and α, and these were shown to agree with the values determined from magnetic susceptibility measurements.

Acknowledgements

I would like to thank my supervisor and consummate researcher, Professor J. C. Woolley, for his advice and help in writing this thesis.

I would also like to thank Professor G. Lamarche for the use of his magnetic susceptibility apparatus, and for being there late at night until all the measurements were completed.

I would like to thank Professor A. Manoogian for discussions with him and hope that his convalescence will be speedy.

I would also like to thank Dr. Tom Donofrio for sharing his savvy in computer programming as well as other subjects with me, and for his diagram of the magnetic susceptibility apparatus.

Thanks also to Bei Wah Chan for making the ESR measurements.

Thanks also goes to my friend Diane for her help in typing this thesis.

Finally, I would especially like to thank my friends, Dan, Pillay, Louis, Germain, John, Andrew, Bruno, Sudershan, Greg, Samir B., Munkid and Riccardo who have made the lunch period much more physically healthy.

CONTENTS

List of Figures

List of Tables

CHAPTER 1 INTRODUCTION

1.1 Background

This thesis deals with materials which have attracted considerable interest recently, Semimagnetic Semiconductor (SMSC) alloys. These materials are formed by alloying ordinary semiconductors with magnetic semiconductors, ie. by substituting cations of ordinary semiconductors with paramagnetic ions of magnetic semiconductors.

It is the introduction of the magnetic component in the semiconductor lattice which causes differences in the semiconductor behaviour from that of a normal semiconductor. One such difference, which is the most striking signature in these SMSC alloys is the spin-glass behaviour, which shows up as a cusp in the magnetic susceptibility measurements. This thesis investigates the spin-glass phenomenon with magnetic susceptibility measurements and attempts to interprete the results by considering some type of exchange interaction between the localized moments and the mobile band electrons.

Most of the earlier work on these SMSC 's has been concerned with pseudobinary alloy systems such as $Cd_{1-z}Mn_zTe$, $Hg_{1-z}Mn_zTe$, $Zn_{1-z}Mn_zTe$, and $Cd_{1-z}Mn_zSe$, etc. and with pseudoternary alloy systems such as $Cd_{1-z}Mn_zTe_{1-y}Se_y$, $Cd_xZn_yMn_zTe$, and $Cd_xZn_yMn_zSe$, etc. However, the research on SMSC 's has been extended at the University of Ottawa, to include pseudoternary alloy systems which crystallize in a structure other than those investigated previously, ie. the chalcopyrite structure.

Some of these systems that have been investigated at the University of

Ottawa are: $Cd_{2x}(CuIn)_yMn_{2z}Te_2$ (86Q1), $Cd_{2x}(AgIn)_yMn_{2z}Te_2$ (85Q3), $Zn_{2x}(CuIn)_yMn_{2z}Te_2$ (87N1), and $Cd_{2x}(AgGa)_yMn_{2z}Te_2$ (87A1). In this thesis, the research deals with the semimagnetic properties of another pseudoternary alloy system, $Cd_{2x}(CuGa)_yMn_{2z}Te_2$.

1.2 Graphical Representation of the Alloy System

To represent any sample concentration of the pseudo-ternary alloy system $Cd_{2x}(CuGa)_yMn_{2z}Te_2$ with $x+y+z = 1$, an equilateral triangular graph may be used, figure 1.1. On this graph, the compounds CdTe, $CuGaTe_2$ and MnTe are located at the x, y and z corners, respectively. The coordinates (x, y, z) or the concentrations of any alloy composition are determined from perpendicular bisectors which are drawn from the corners of the triangle. To obtain the whole range of alloy compositions, the perpendicular bisectors are scaled from 100% at the corners to 0% at the base. For example, the point drawn on the figure 1.1 represents 25% CdTe, 25% $CuGaTe_2$ and 50% MnTe. Parenthetically, it is worth noting that this is equivalent to 25% Cd, 25% CuGa (or 12.5% Cu, 12.5% Ga) and to 50% Mn for the cations; and to 100% Te for the anions. Thus, concentrations of any alloy composition can be thought of as concentrations of cations, and may be written as 25/25/50.

Three binary systems are also represented along the edges of the triangle in figure 1.1. These are: $Cd_{1-z}Mn_zTe$, $Cd_{2(1-y)}(CuGa)_yTe_2$ and $(CuGa)_{1-z}Mn_{2z}Te_2$. The former system was analysed extensively by Brun del Re et al. (83B1), by Triboulet and Didier (81T1) and by Galazka (79G1). Thus no work has been done here on

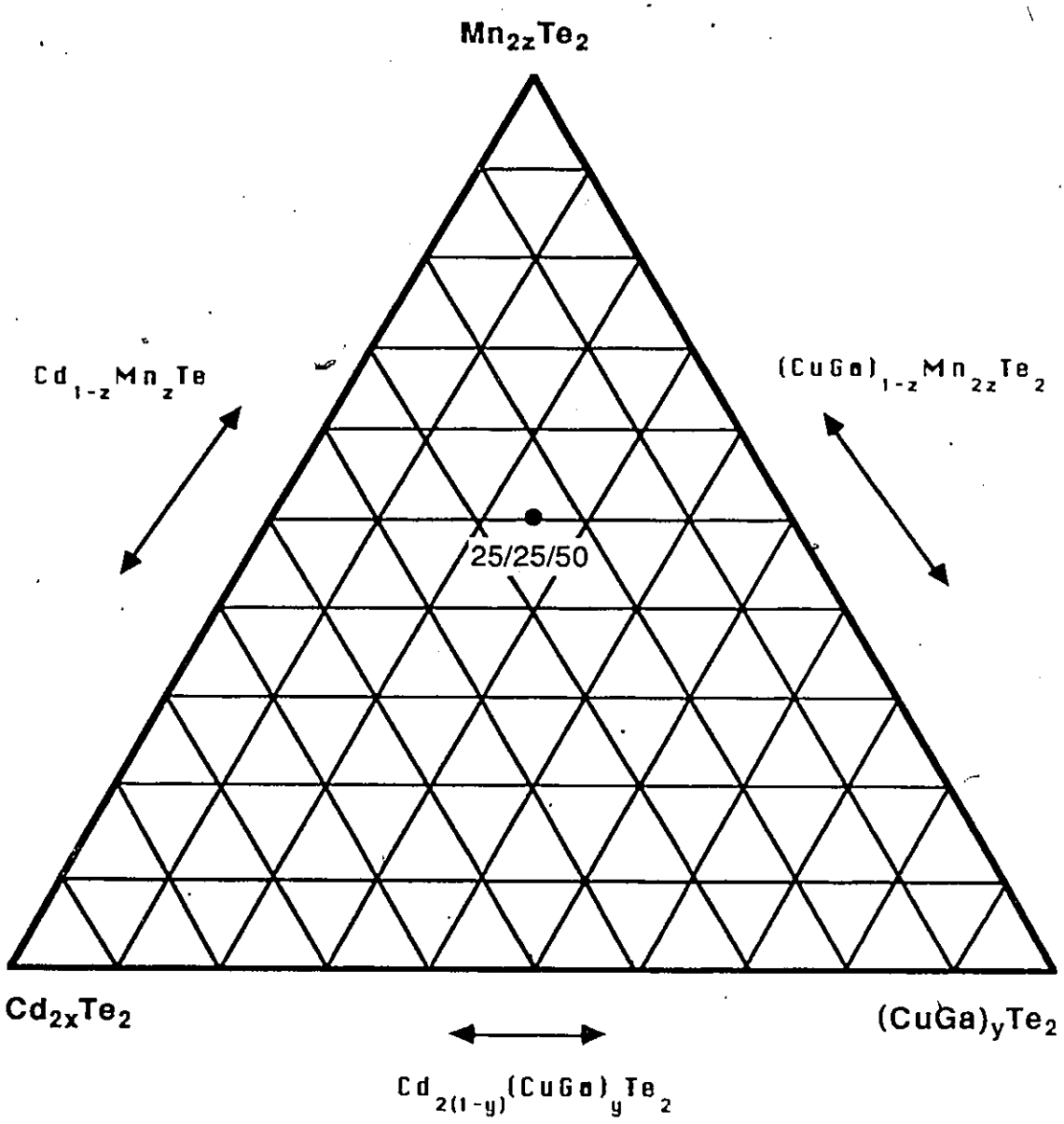

FIGURE 1.1 Graphical representation of the $Cd_{2x}(CuGa)_yMn_{2z}Te_2$ alloy system with $x + y + z = 1$. Three binary systems and the coordinates of the 25/25/50 composition are also indicated.

this binary system. The second system was analysed by Woolley and Williams (66W1) and again no work has been done here, although the results were used to corroborate the results of this present investigation. The last system has not been analysed anywhere and is part of this investigation. This binary system is in fact part of an investigation on chalcopyrite alloys of the form $(I\ III)_{1-z}Mn_{2z}Te_2$ with I = Cu, Ag and III = In, Ga as reported by Woolley et al. (87W1).

To obtain a representative set of samples for the present system, compositions are chosen from a grid of the equilateral triangle in figure 1.1, see figure 1.2. In this figure, the horizontal lines represent compositions of constant manganese concentration and the vertical lines represent constant f ratio, ie. constant copper+gallium to copper+gallium+cadmium ratio, or y / x+y. This grid also permits the analysis of various properties to be made as a function of a single variable. For example, investigations of the lattice structure, energy gap, ESR linewidth and magnetic susceptibility can be carried out as a function of f ratio and as a function of z, the manganese concentration.

The format of this thesis is as follows. In chapter 2, crystallographic results by the Debye-Scherrer x-ray analysis reveal an isothermal section for the system with, however, some uncertainties near the chalcopyrite field. In chapter 3, optical energy gap measurements are carried out on the single phase samples determined from crystallographic analysis. In chapter 4 and 5, magnetic properties in the presence of a magnetic field are investigated by ESR and low-field susceptibility, respectively.

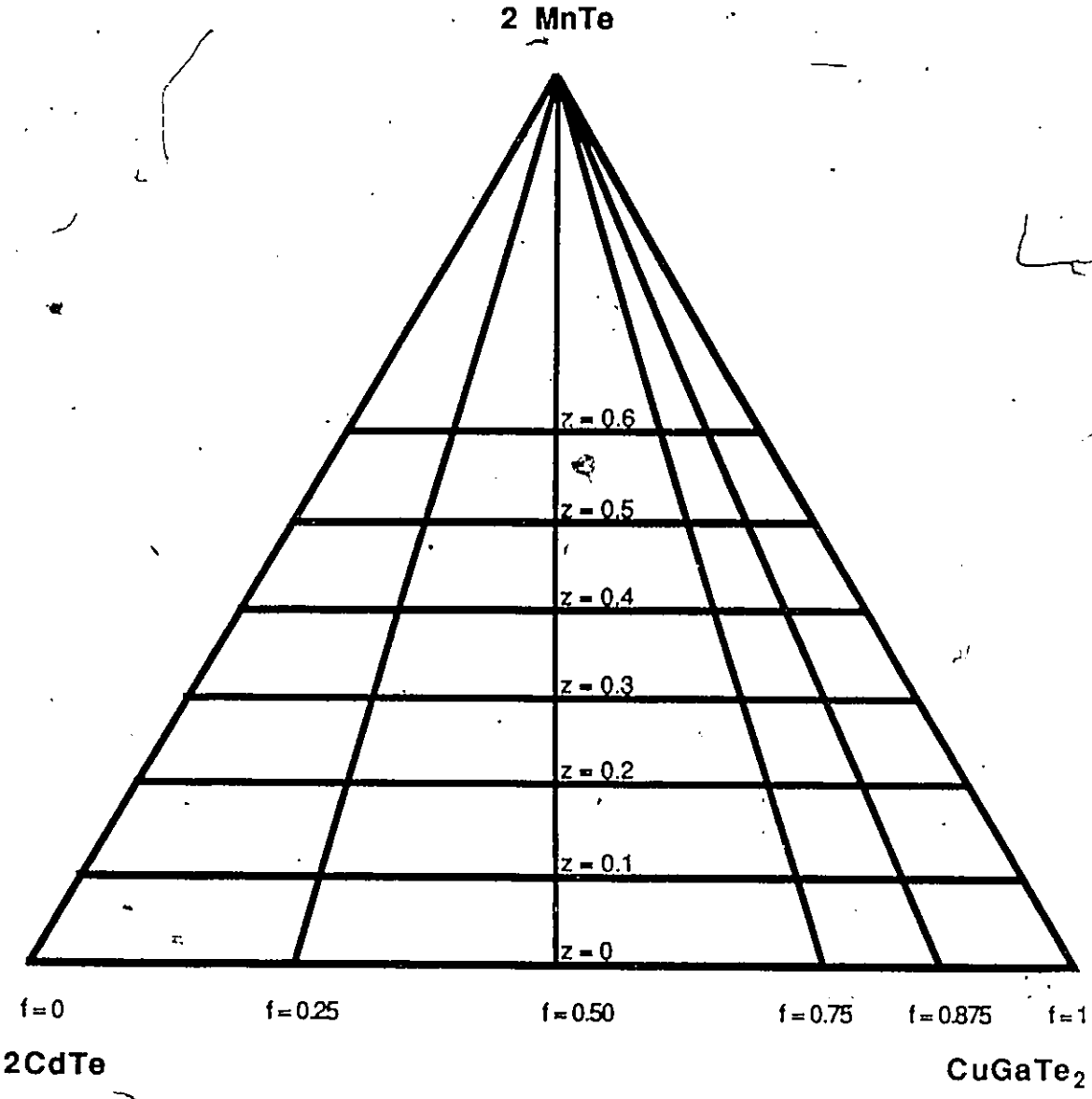

FIGURE 1.2 Representative set of samples for the $Cd_{2x}(CuGa)_yMn_{2z}Te_2$ alloy system.

CHAPTER 2 CRYSTALLOGRAPHIC ANALYSIS

2.1 Introduction

In this chapter, lattice parameter results obtained by the Debye-Scherrer powder diffraction method on polycrystalline samples of the $Cd_{2x}(CuGa)_yMn_{2z}Te_2$ system that were prepared from pure elements are presented. However, because the samples near the chalcopyrite phase field did not achieve equilibrium, the above crystallographic analysis is not complete. As a consequence of this, only an attempted phase condition can be drawn from the above incomplete crystallographic analysis.

However, Quintero et al. (87Q1) measured a T(z) phase diagram of the edge $(CuGa)_{1-z}Mn_{2z}Te_2$ (figure 1.1) by differential thermal analysis (DTA) and this is used to bring modifications to the above attempted isothermal section. The DTA measurements were performed at Universidad de Los Andes, Merida, Venezuela by Quintero et al. in collaboration with Professor Woolley on the same samples that were prepared for this present research.

2.2 Sample Preparation

Some 40 polycrystalline samples were produced by the melt and anneal technique. In this method, appropriate amounts of each element are melted in an evacuated quartz ampoule at 1150 ± 30 °C for one to two hours, annealed for fifteen days at 750 ± 20 °C and then quenched in water. (However, the choice of the annealing temperature became more complicated for some samples because different annealing temperatures produced different phase conditions. This is why only

an attempted isothermal section was possible. This is discussed later.)

Gallium, one of the elements of the system, however, proved to be very unmanageable during weighing, ie. it melted below 29 °C and was difficult to cut. Therefore the compound Ga_2Te_3 was used to provide the required molar fractions of gallium for each composition rather than elemental gallium. In this way, gallium was weighed twice to produce two ten gram samples of Ga_2Te_3 rather than some forty times for the individual alloys. Because the atomic ratio of tellurium to gallium in Ga_2Te_3 was always less than that of any composition of the system, elemental tellurium always had to be added to satisfy its molar requirement for each composition.

In order to find the masses of the constituent elements and Ga_2Te_3 required for each one gram sample, a computer program was written. The masses were calculated to a precision of 0.1 mg and the measurements were made on a balance to a precision of 0.2 mg.

During the melting process, the quartz ampoule was found to react with the melt. To inhibit this reaction, carbonization, the deposition of a carbon layer on the inside walls of the ampoule was found to be necessary. Carbon is produced by cracking acetone at high temperatures according to the following reaction:

$$(CH_3)_2C{=}O + \text{HEAT} \longrightarrow 2C + CH_4 + H_2O \qquad \text{(equation 2.1)}$$

To obtain this reaction, acetone vapours had to be contained inside an open end quartz tube before any heat was applied. This was done by inserting a tightly rolled-up paper towel inside a quartz tube containing 2-3 ml of acetone and by tipping the tube until the paper was soaked by all the acetone. The acetone vapours needed for the reaction were supplied by the wet paper. A deposition of carbon on

the inside walls of the tube was now created by heating the outside of the tube with the oxy-acetylene torch. The deposition, however, was limited to the tip of the flame so that rotating the tube in a screw-like overlapping fashion over the flame ensured a uniform deposition of carbon. This deposition typically ran from the bottom of the tube up to about 2.5 cm inside a tube of length 7-8 cm. The diameter of the tube was 5 mm and the walls were 1 mm in thickness.

The choice of a melting temperature at 1150 ± 30 °C was guided by the melting temperatures of the elements and the compounds involved and by the temperature at which the furnace winding would melt. The melting temperature of the elements and the compounds are listed in the following table.

Table 2.1 Melting Temperatures of elements and compounds.

Element	Melting Temperature (°C)	Compound	Melting Temperature (°C)
Ga	29	Ga_2Te_3	790
Cd	320.8	$CuGaTe_2$	870
Cu	1083	CdTe	1098
Mn	1220	MnTe	1165
Te	453		

Because the melting temperature of 1150 ± 30 °C did not exceed that of every compound and element, the samples were shaken periodically for 1-2 hours at that melting temperature in order to dissolve the compounds and the elements in the

melt. The result was that some degree of homogeneity was attained. The samples were then transferred to another furnace to anneal for fifteen days.

The cooling treatment of these samples after removal from the annealing furnace turned out to be of considerable importance. Initially, the samples were allowed to cool in the furnace to room temperature which resulted in a very slow rate of cooling. This permitted the possibility of phase changes occurring during the cooling treatment because it was discovered later that different phases were possible for some samples depending on the annealing temperature. Hence, to try to prevent any phase changes, the samples were quenched in water to give as quick a cooling as possible.

Also, since different annealing temperatures produced different phase conditions, not all the samples could not be obtained in a single phase equilibrium state because the annealing temperature for some samples remained unknown. A complete phase diagram of the system could provide such information.

After this work had been completed and the thesis was being written, Quintero et al. (87Q1) measured a T(z) phase diagram on the same samples of the $(CuGa)_{1-z}Mn_{2z}Te_2$ edge. From this diagram, a better insight can be obtained for the annealing temperature for those samples but lack of time prevented further analysis to be made.

The samples which were in a single phase equilibrium state were then analysed by the Debye-Scherrer diffraction method to determine the crystal structure and the lattice parameter(s).

2.3 X-ray Analysis

The crystallographic structures expected in the present system are those of the compounds at the corners of the triangle: zinc blende for CdTe, chalcopyrite for $CuGaTe_2$ and hexagonal nickel arsenide for MnTe. However, because the solid solution of the hexagonal nickel arsenide phase characteristically extends to about 1-2% (85C1) in these systems and because it does not form a spin glass, its structure will not be discussed here.

The zinc blende structure has two interpenetrating face centered cubic lattices which are offset with respect to one another by one quarter body diagonal, figure 2.1. One lattice is occupied by tellurium anions and the other is occupied by a random distribution of Cd, Ga, Cu, and Mn cations. The arrangement is such that each cation is tetrahedrally bonded to four anions and each anion is tetrahedrally bonded to four cations without any ordering. The type of bonding involved is covalent with some degree of ionicity.

However, if ordering of the cations I = Cu and III = Ga occurs in the zinc blende structure, then a chalcopyrite or body centered tetragonal structure results, figure 2.2. In this structure, two sublattices are occupied by cations of element I = Cu and III = Ga and the other sublattice by anions of element VI = Te. The arrangement is such that each I and III cation is tetrahedrally bonded to four VI anions, but that each VI anion is tetrahedrally bonded to two I cations and two III cations. Since cations I and III have different ionicity and hence bond strength, a compression along the z axis results, causing $c / a < 2$.

The Debye-Scherrer powder method consists of grinding a specimen to a fine powder, applying it to a glass holder with grease and exposing the sample to Cu $K_{\alpha 1}$ radiation in a camera for 6 hours. After exposure, the lattice parameters can be

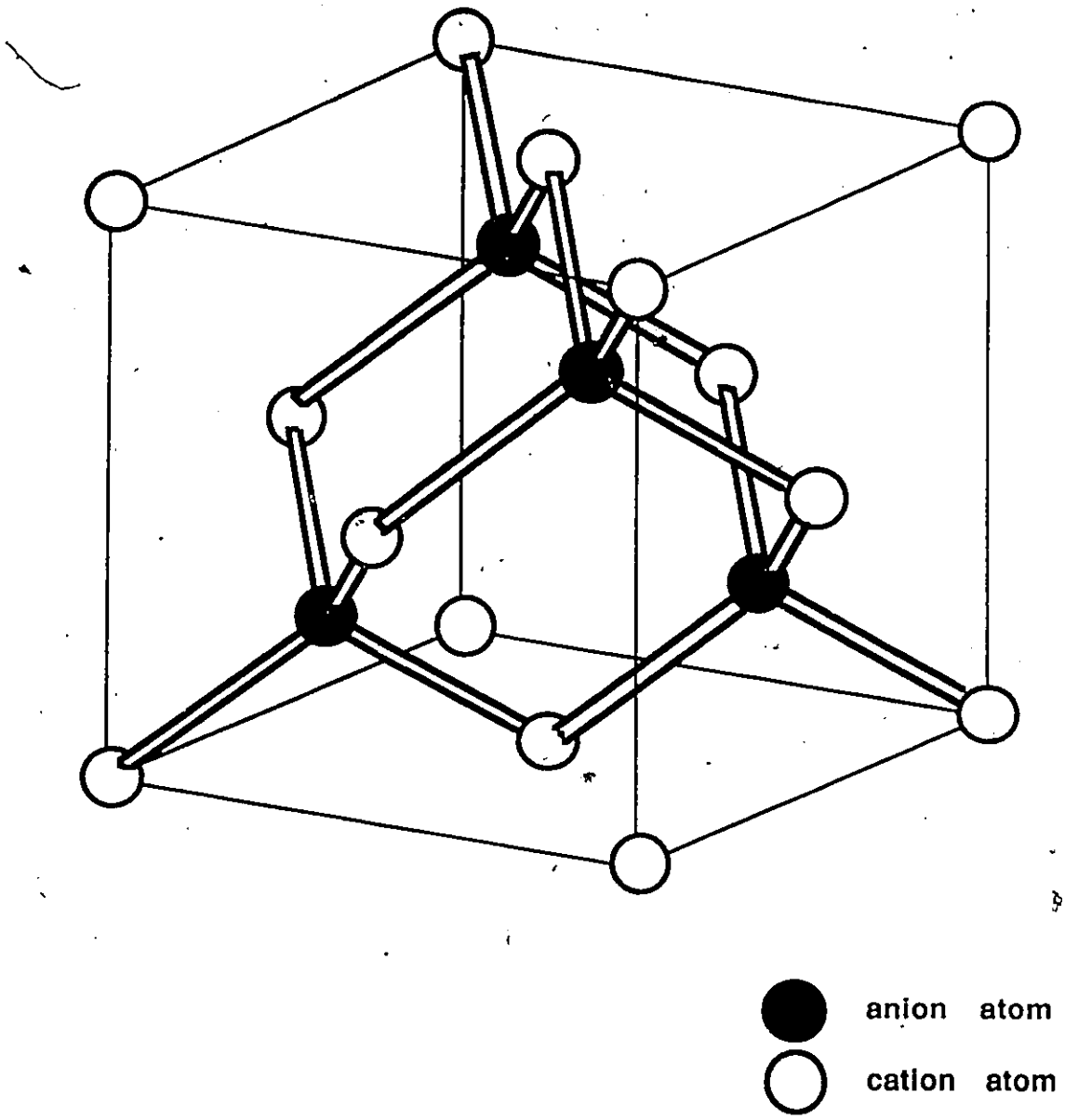

FIGURE 2.1 Drawing of the zinc blende structure.

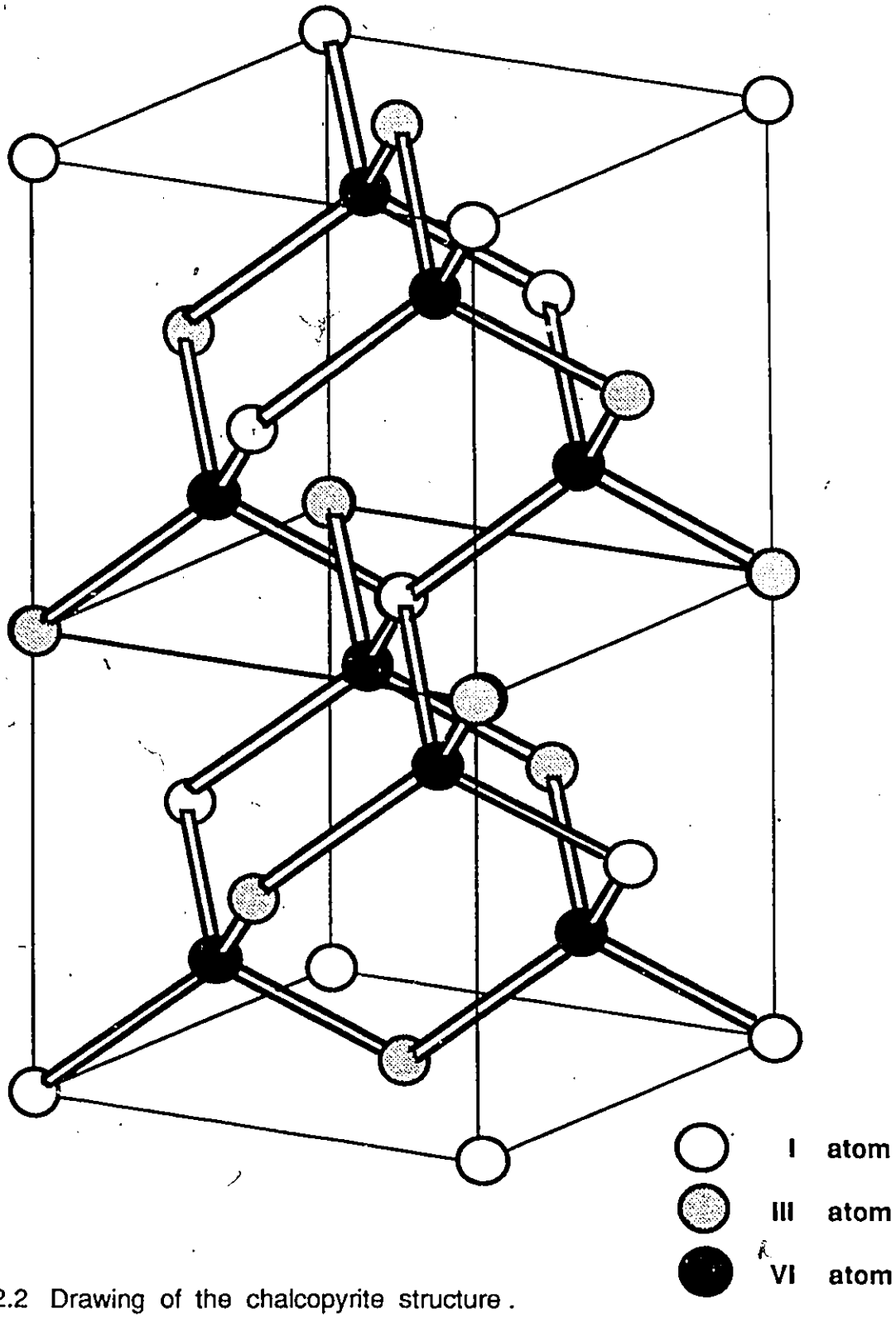

FIGURE 2.2 Drawing of the chalcopyrite structure.

determined by measuring the position of the diffracted lines on the film and by determining the corresponding Bragg angles, θ.

For cubic symmetry, the general Bragg reflection condition is:

$$\sin^2\theta = \frac{\lambda^2 N}{4a^2} \qquad \text{with } N = h^2 + k^2 + l^2 \qquad \text{(equation 2.2)}$$

where θ is the Bragg angle

λ = 0.15405 nm for Cu $K_{\alpha 1}$ radiation

h, k, l are the Miller indices

and a is the lattice parameter

For the zinc blende structure, which belongs to the f.c.c. point group, strong reflection occurs for N = 3, 11, 16, 19, 24, etc. and weak reflection for N = 4, 12, 20, etc. (85Q1). Having determined the lattice parameter values for the lines indexed with the proper Miller indices, the Nelson-Riley extrapolation method (45N1) is used to obtain the true lattice parameter. In this method, the lattice parameter for each Bragg angle is plotted as a function of f(θ), equation 2.3.

$$f(\theta) = \frac{1}{2}\left(\frac{\cos^2\theta}{\sin\theta} + \frac{\cos^2\theta}{\theta}\right) \qquad \text{(equation 2.3)}$$

This function, f(θ), corrects for the absorption due to the finite dimensions of the specimen on the holder. The true lattice parameter is obtained by extrapolating to f(θ) = 0, see figure 2.3.

For tetragonal symmetry, the general Bragg reflection condition is:

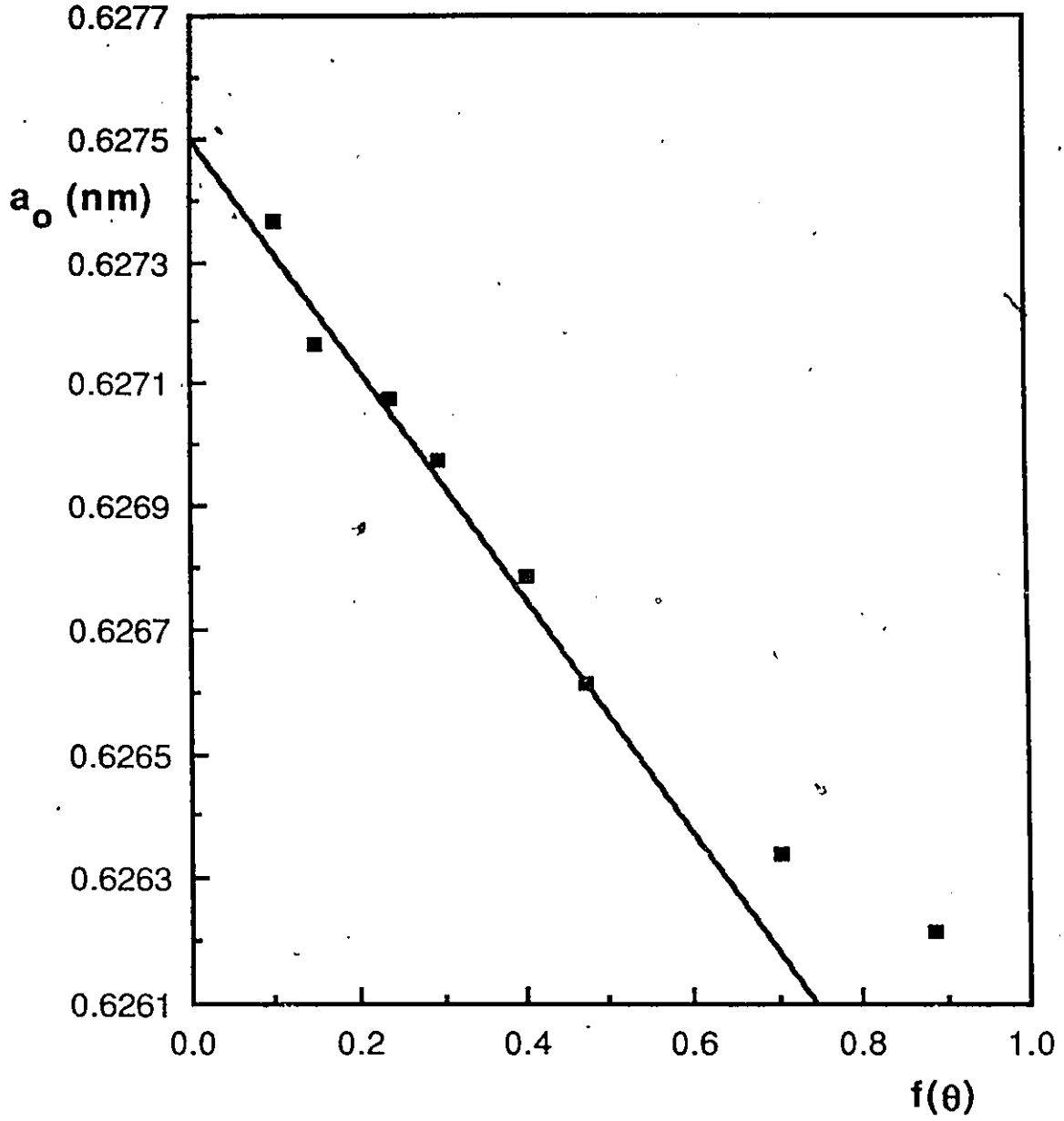

FIGURE 2.3 Determination of the lattice parameter by the Nelson-Riley extrapolation method for the sample 35/35/30 whose structure is zinc blende.

$$\sin^2\theta = \frac{\lambda^2}{4}\left(\frac{h^2+k^2}{a^2}+\frac{l^2}{c^2}\right) \qquad \text{(equation 2.4)}$$

where θ is the Bragg angle

λ = 0.15405 nm for Cu $K_{\alpha 1}$ radiation

h, k, l are the Miller indices

and a and c are the lattice parameters

The indices of the chalcopyrite structure may be derived from the zinc blende indices because the atomic sites in the chalcopyrite structure have the same positions as in the zinc blende structure when c / a = 2. Following the method by Quintero (85Q2) and Yoodee (85Y1), the index l_{zb} of zinc blende is doubled to obtain the index l_{ch} of chalcopyrite, the indices h and k being the same. For example, with N = 11, the Miller index of the zinc blende is (311) and that of the chalcopyrite is (312) and (116), since the index l_{zb} of the zinc blende could be 1 and 3, respectively. When c / a = 2, however, the 312 and 116 diffraction lines occur at exactly the same angle θ. Only when c / a < 2 do the lines split showing two diffraction lines. The Miller indices for the chalcopyrite and the zinc blende structures are listed in table 2.2.

Having determined θ, the Bragg angle from the x-ray film and having established the Miller index for each diffraction line, the lattice parameters a and c are then determined by a least squares fit to equation 2.4.

Since smooth variation of lattice parameter values along any line (ie. along f and z in figure 1.2) occurs only in single phase regions, the boundaries between single and two phase regions may be determined from discontinuities along any line.

Table 2.2 Miller Indices for Zinc Blende and Chalcopyrite Structures.

Zinc Blende		Chalcopyrite
N	h k l	h k l
3	1 1 1	1 1 2
4	2 0 0	2 0 0 0 0 4
8	2 2 0	2 2 0 2 0 4
11	3 1 1	3 1 2 1 1 6
12	2 2 2	2 2 4
16	4 0 0	4 0 0 0 0 8
19	3 3 1	3 3 2 3 1 6
20	4 2 0	4 2 0 4 0 4 2 0 8
24	4 2 2	4 2 4 2 2 8
27	3 3 3 5 1 1	3 3 6 5 1 2 1 1 10
32	4 4 0	4 4 0 4 0 8
35	5 3 1	5 3 2 5 1 6 3 1 10
36	6 0 0	6 0 0 0 0 12
40	6 2 0	6 2 0 6 0 4 2 0 12
43	5 3 3	5 3 6 3 3 10
44	6 2 2	6 2 4 2 2 12
48	4 4 4	4 4 8
51	7 1 1 5 5 1	7 1 2 1 1 14 5 5 2 5 1 10
52	6 4 0	6 4 0 4 0 12 6 0 8
56	6 4 2	6 4 4 4 2 12 6 2 8
59	7 3 1 5 5 3	3 1 14 7 3 2 7 1 6 5 5 6 5 3 10

2.4 Results and Discussion

Measurements of lattice parameter were made on the samples chosen from the grid of this system, figure 1.2. The results of the lattice parameter, a, as a function of z concentration are shown in figure 2.4. In this figure, estimates of the boundaries of the two phase regions are made based on:

i) results obtained from Woolley and Williams (66W1) on the extent of the solid solution in $Cd_{2(1-y)}(CuGa)_yTe_2$ (z = 0 in figure 2.4),

ii) results obtained from Brun del Re et al. (83B1) on the extent of the solid solution in $Cd_{1-z}Mn_zTe$ (f = 0 in figure 2.4),

iii) discontinuities in the linearity of lattice parameter values as a function of manganese concentration, and

iv) the inability to obtain good equilibrium conditions for the samples inside the zinc blende + chalcopyrite region due to a lack of knowledge of the phase diagram.

These results will be used later to represent an attempted phase condition for the alloy system when annealed at 750 °C and quenched to room temperature.

Figure 2.5 shows the variation of the lattice parameter, a, with f ratio for lines of constant manganese concentration. In this figure, it can be seen that as a general rule, the lattice parameter decreases with increasing f ratio. This will become important in subsequent chapters when the distance between magnetic ions becomes important. Because of the compactness of figure 2.5, no indication of the phase boundaries involved can be possible. However, figure 2.4 provides a good picture of the phases involved and these may be translated to represent an attempted phase condition of the system, see figure 2.6.

In this figure, the extents of the single phase fields, zinc blende and

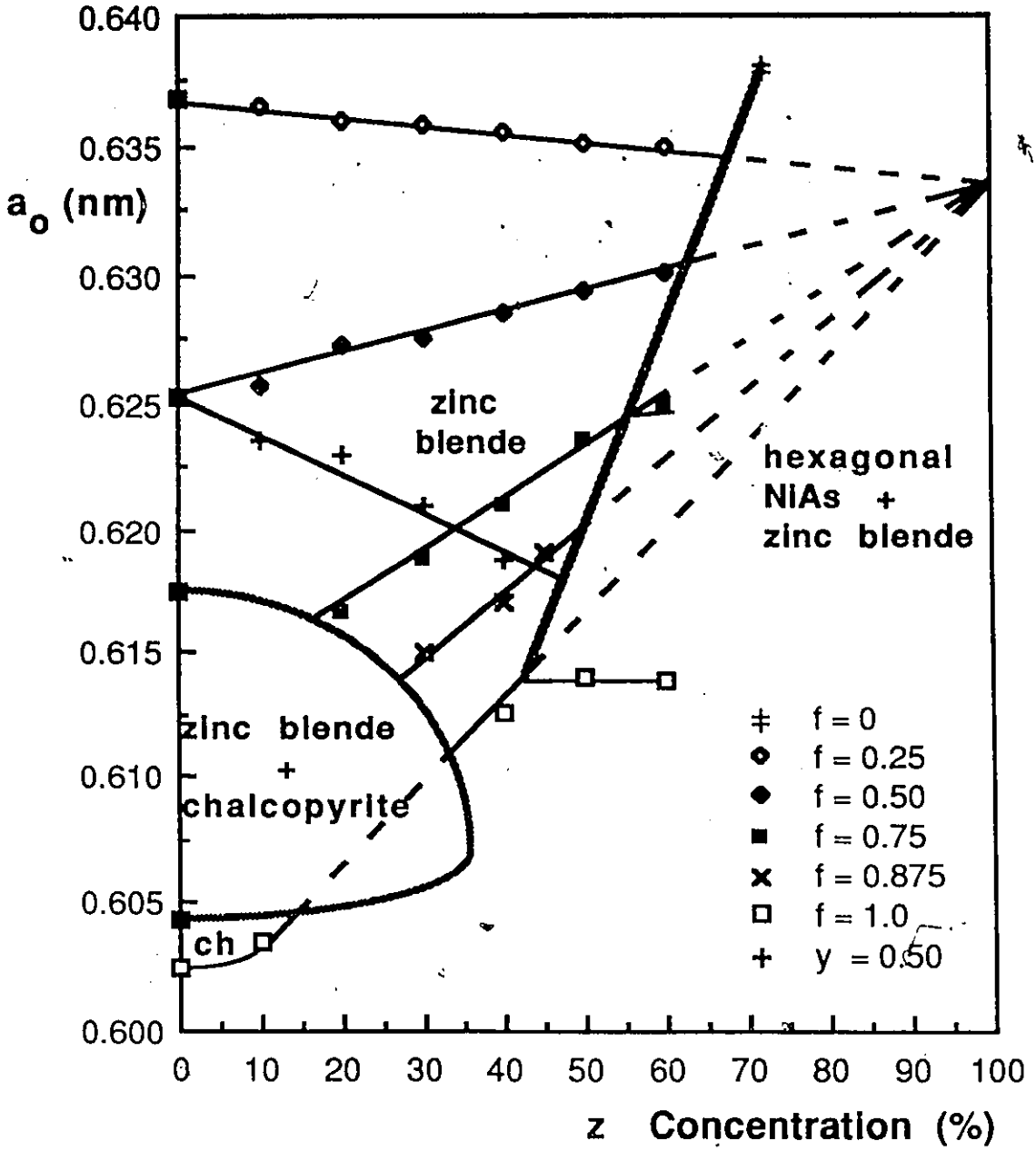

FIGURE 2.4 Lattice parameter values of the alloy system $Cd_{2x}(CuGa)_yMn_{2z}Te_2$ as a function of z concentration, where f=y/x+y. The points at z=0 are taken from Woolley and Williams (66W1). The point for f=0 which delimits the two phase field is taken from Donofrio (86D1).

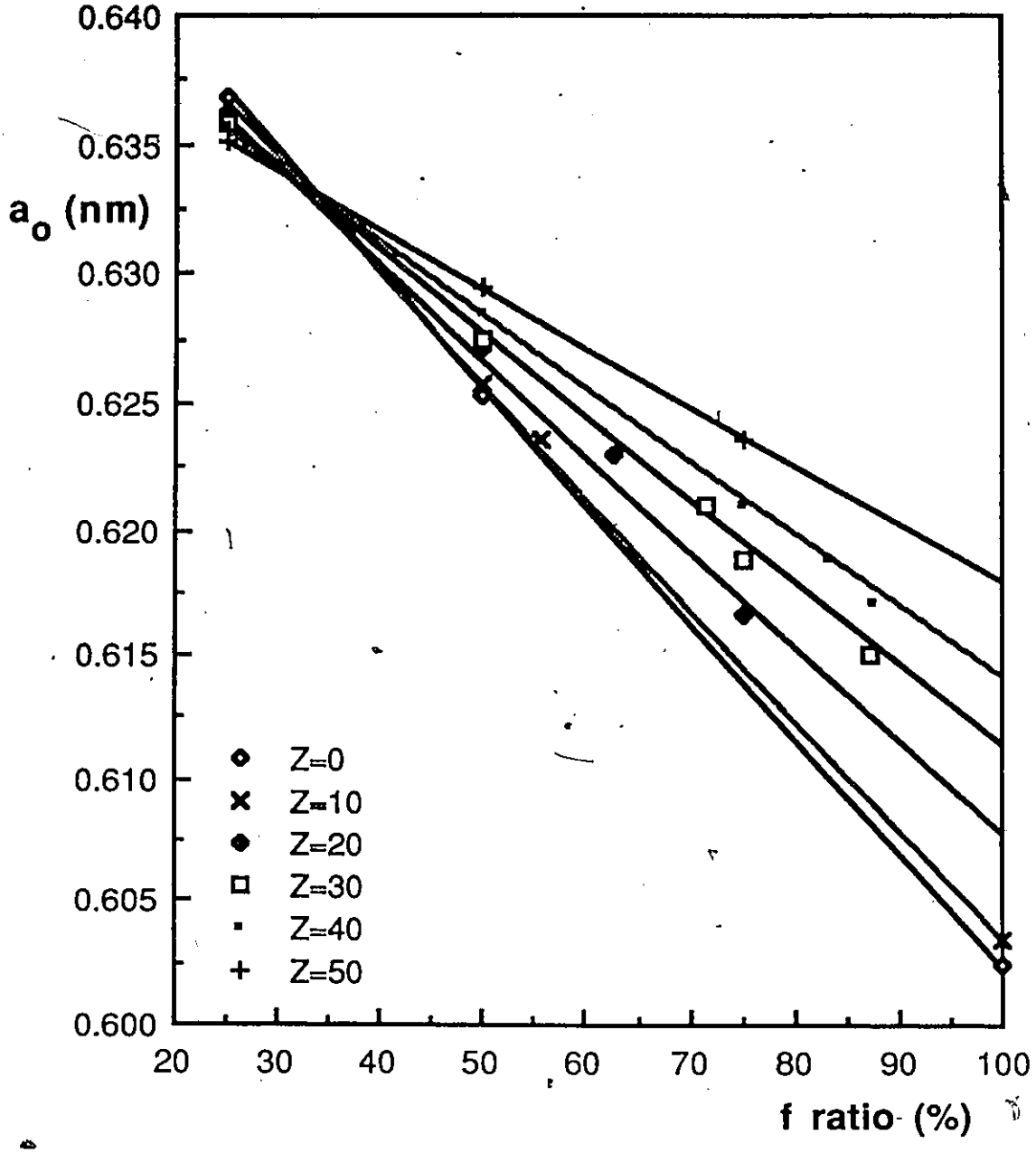

FIGURE 2.5 Lattice parameter values of the alloy system $Cd_{2x}(CuGa)_yMn_{2z}Te_2$ as a function of $f=y/x+y$ for constant z concentrations.

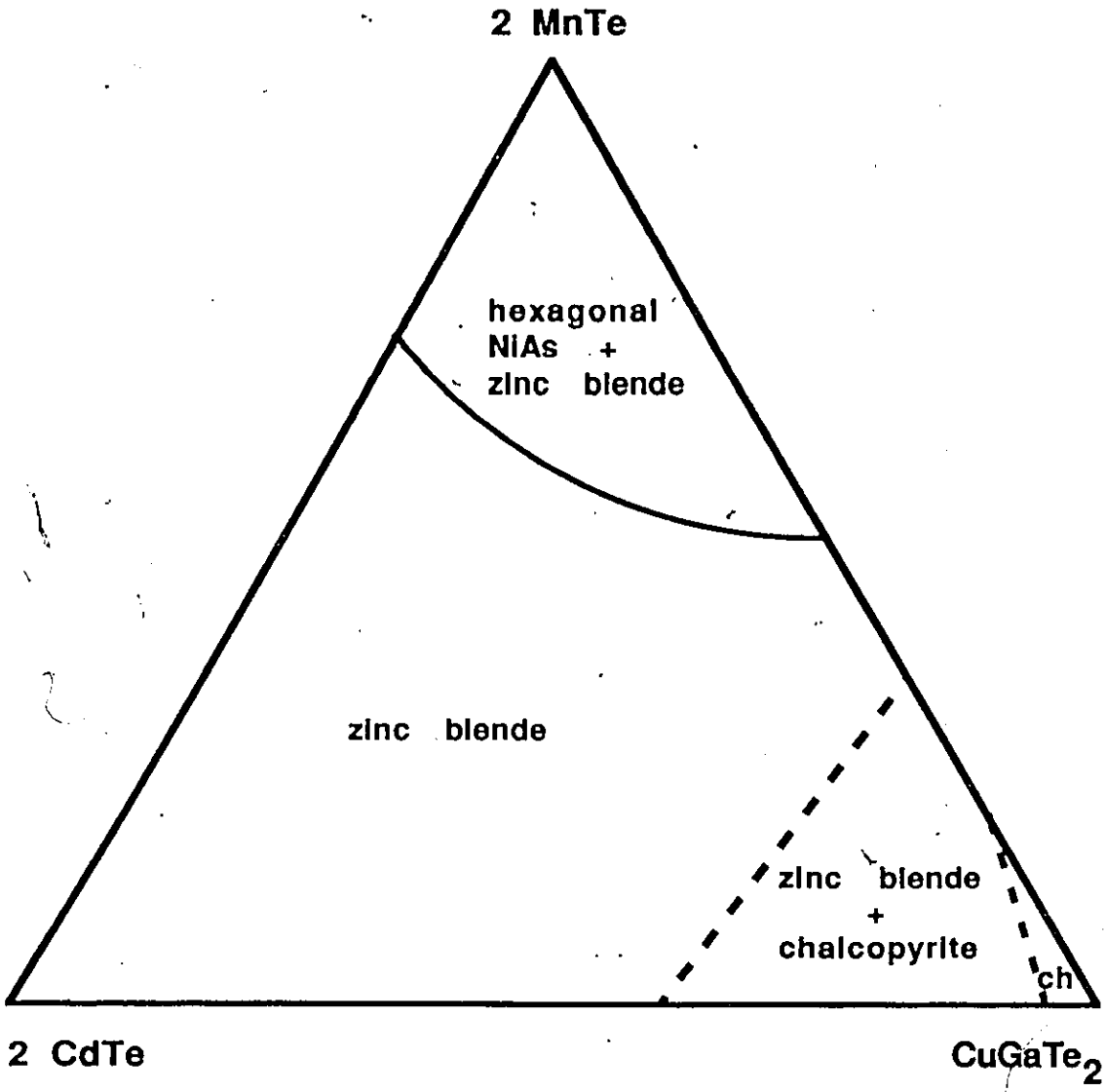

FIGURE 2.6 Estimated phase condition of the $Cd_{2x}(CuGa)_yMn_{2x}Te_2$ alloy system drawn from crystallographic analysis of samples annealed at 750°C and quenched to room temperature.

chalcopyrite, are shown along with both two phase fields, (MnTe + zb) and (zb + ch). Again, the extent of the two phase field (zb + ch) up to the x = 0 edge is due to the fact that the samples did not achieve equilibrium which is because of the suspected complicated phase diagram in that area. In order to obtain a more accurate form for figure 2.6, a complete phase diagram of the system would be required and that in itself is enough work for another research, according to Professor Woolley.

Recently, however, after the above work had been completed and the thesis was being written, Quintero et al. (87Q1) measured a T(z) phase diagram of the edge $(CuGa)_{1-z}Mn_{2z}Te_2$ with the same samples used for this investigation. figure 2.7. In this figure, the various phases involved for $0 \leq z \leq 0.6$ are presented. Some of the important structures involved in this T(z) phase diagram are: α' which represents Mn-ordered chalcopyrite structure, α which represents Mn-disordered chalcopyrite structure, β and β_1 which represent zinc blende structures of different compositions, and γ which represents the NiAs hexagonal structure. Most importantly, this figure may be used to modify the attempted phase condition of figure 2.6.

It is seen in figure 2.7 that for T < 550 °C, no zinc blende phase and no zinc blende + chalcopyrite field are present in that section. Hence, the phase condition of the $Cd_{2x}(CuGa)_yMn_{2z}Te_2$ alloy system for T < 550 °C is more likely to be of the approximate form shown in figure 2.8.

In this figure, the chalcopyrite phase field is seen to increase up to 40% along the edge, and the two phase field (zb + ch) is seen to decrease towards the bottom of the diagram. The extent of these phases, however, towards the interior are approximate and other DTA measurements should give more acurate results.

Having obtained an approximate phase condition from various sources, this figure is further modified as a result of optical energy gap measurements as described in chapter 3.

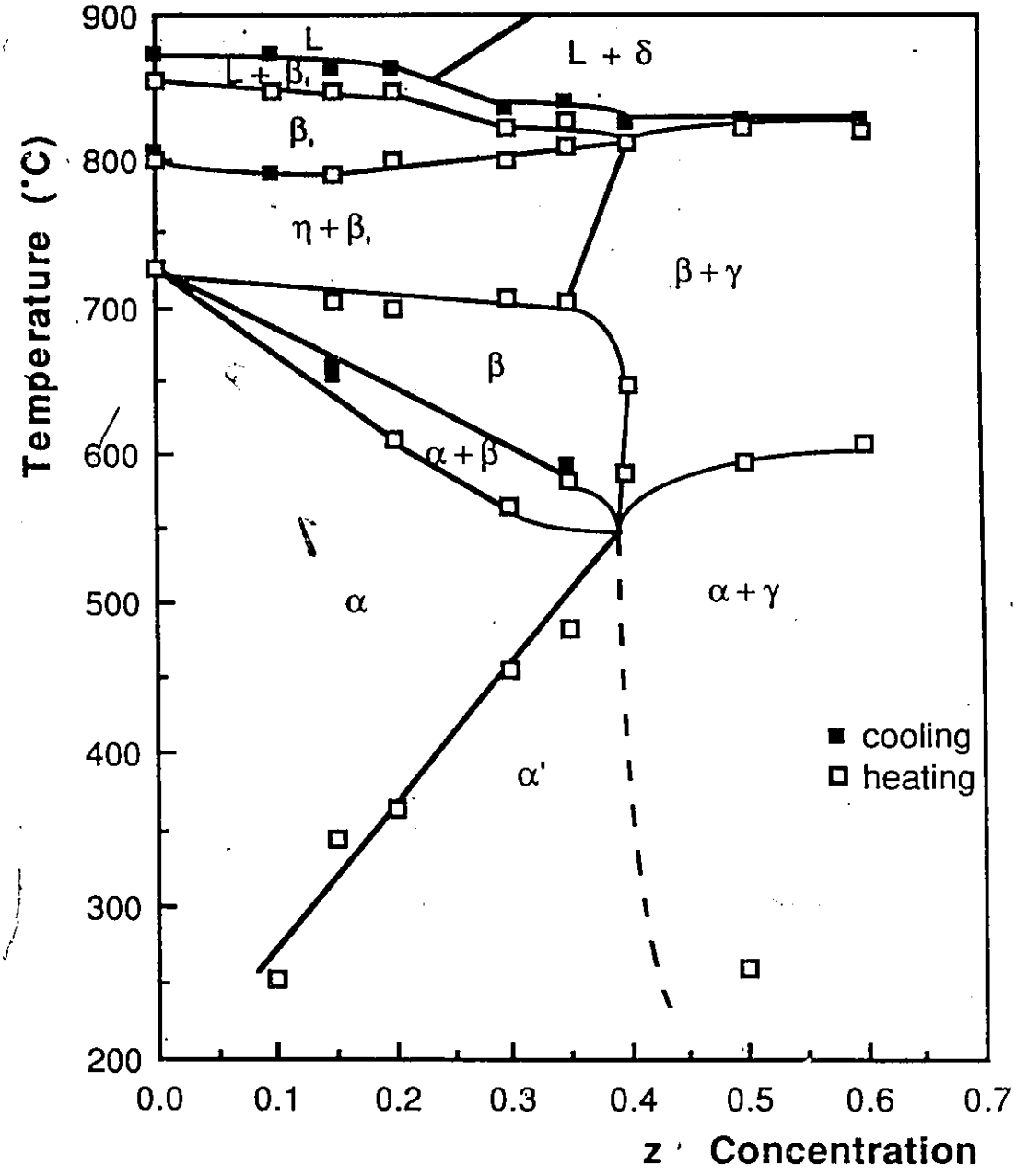

FIGURE 2.7 Measured T(z) phase diagram of the $(CuGa)_{1-z}Mn_{2z}Te_2$ system with $0 \leq z \leq 0.6$ drawn from differential thermal analysis (DTA) by Quintero et al. (87Q1).

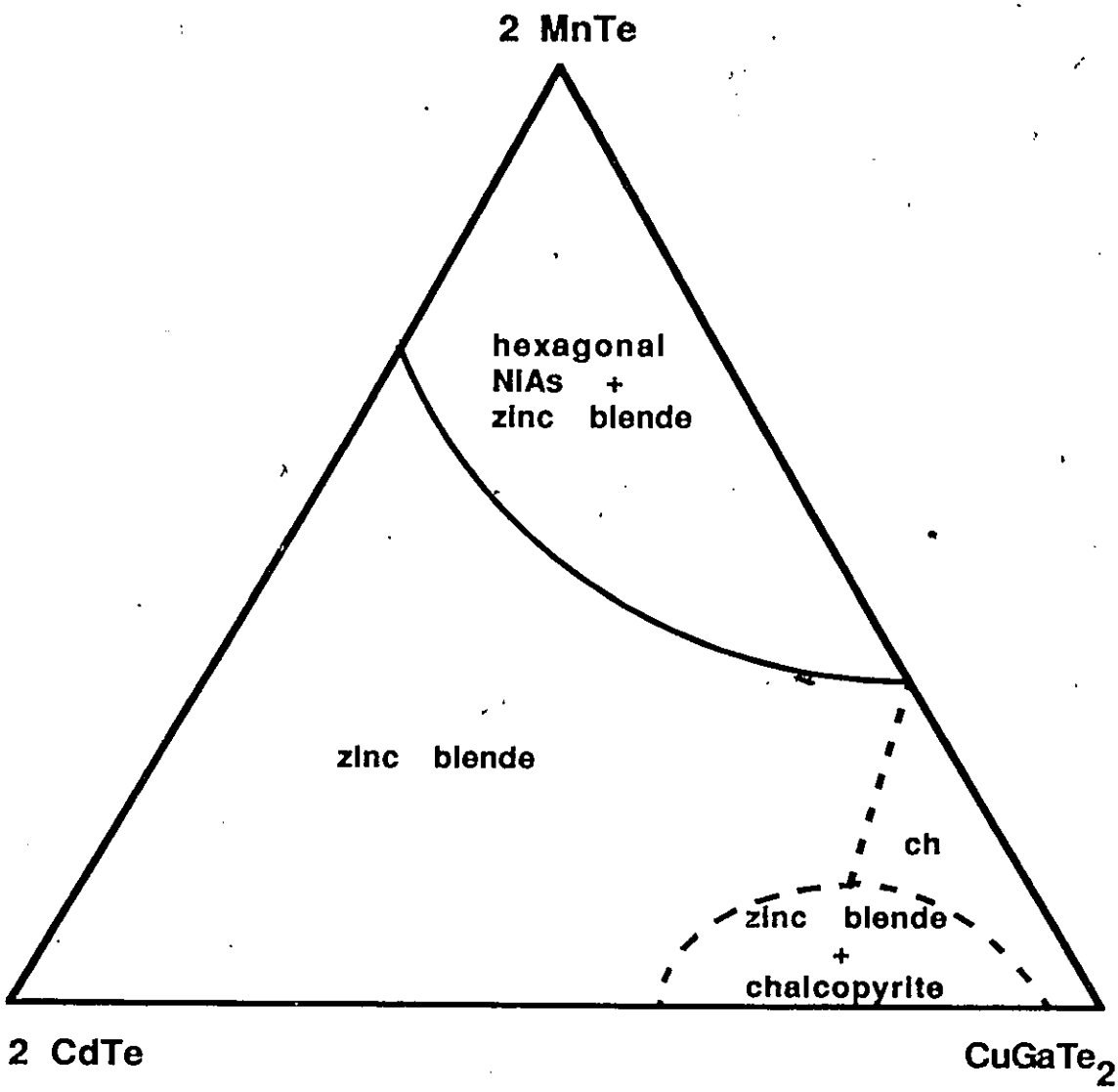

FIGURE 2.8 Estimated phase condition of the $Cd_{2x}(CuGa)_yMn_{2x}Te_2$ alloy system for T<550°C drawn from crystallographic analysis and differential thermal analysis (DTA).

CHAPTER 3 OPTICAL ABSORPTION

3.1 Introduction

In this chapter, energy band gap results by optical absorption at the fundamental edge are presented. The procedure followed is described by Goodchild et al. (82G1). From the graphs of energy band gap against z and y concentration, the phase diagram drawn from crystallographic analysis and DTA results in the previous chapter is modified to include an 'ordered' zinc blende structure as was previously reported by Quintero et al. in the alloy systems $Cd_{2x}(AgIn)_yMn_{2z}Te_2$ (85Q3) and $Cd_{2x}(CuIn)_yMn_{2z}Te_2$ (86Q1).

3.2 Theory

Optical energy band gap results were obtained on single phase samples of the $Cd_{2x}(CuGa)_yMn_{2z}Te_2$ system by following the method described by Goodchild et al. (82G1). In this method, the energy gap is determined from the relation of the absorption coefficient and the photon energy at the absorption edge (79P1):

$$\alpha h\nu = A (h\nu - E_g)^n \qquad \text{(equation 3.1)}$$

where α is the absorption coefficient

$h\nu$ is the photon energy

A is a constant

E_g is the energy band gap

and $n = 1/2$ for direct allowed transition

$n = 2$ for indirect allowed transition

$n = 3/2$ for direct forbidden transition

$n = 3$ for indirect forbidden transition

Hence, from equation 3.1, the value of the energy gap may be determined as a linear extrapolation to the abscissa in a graph of $(\alpha h\nu)^{1/n}$, with a suitable value of n, as a function of $h\nu$, the photon energy. However, in order to draw this graph, the value of α, the absorption coefficient, must be determined as a function of the photon energy.

To do this, the incident and transmitted light intensity, I_O and I_T, are measured on a sample of thickness d for wavelengths near the absorption edge since to a good approximation (68G1, 80H1),

$$I_T = I_O (1 - R^2) \exp (-\alpha d) \qquad \text{(equation 3.2)}$$

where R is the reflectivity and is assumed constant.

It is convenient to rewrite equation 3.2 by taking the natural logarithm to give:

$$\ln\left(\frac{I_T}{I_O}\right) = -\alpha d - \ln k \qquad \text{(equation 3.3)}$$

where k is a constant since R is a constant.

Or, rearranging equation 3.3 in terms of α gives:

$$\alpha = \frac{1}{d} \ln \left(\frac{I_O}{I_T} \right) - b \qquad \text{(equation 3.4)}$$

where b is the background signal + ln k

Thus, from equation 3.4, a graph of 1/d $\ln(I_O / I_T)$, minus an extrapolated background in the appropriate wavelength range near the fundamental edge gives the absorption coefficient as a function of photon energy. Then, the value of the energy gap is determined by a graph of equation 3.1.

3.3 Experiment

The schematic diagram of the apparatus used to measure the energy gap is depicted in figure 3.1. The apparatus consists of a 30 W tungsten ribbon lamp, a chopper with a frequency set at 800 - 900 Hz which is in a quiet part of the external noise spectrum (83H1), a Spex 1702 monochromator with a Bausch and Lomb grating blazed at 1.6 μm which provided wavelengths appropriate for relatively wide gap semiconductors (700 - 1100 nm), a concave mirror which focused the light on a Dumont 6911 photomultiplier which was used as a detector, a PAR-186A lock-in amplifier and a chart recorder.

In order to make measurements of I_O and I_T, adequate transmission of light had to be obtained through the samples. This meant that the specimens had to be made as thin as possible, without breaking them. This was done by cutting the samples into slices and then by grinding down these slices to 30 - 200 μm with silica powder on a rotating polishing table. There were two machines that could be used to cut the samples into slices. One was a wire saw and the other was a rotating disc saw which were both very time consumming.

Riccardo Brun del Re, a graduate student of the same semiconductor lab suggested using the cutters (that were used in the preparation of samples to obtain appropriate weights of the elements) to cleave slices from the ingot. His method worked for samples that did not easily crumble and a lot of time was saved, especially when the sample had to be cut several times because of breakage during the mounting, etc.

The slices were then ground down to thin discs of thickness 30 - 200 μm with the polishing table and silica powder before being mounted on to an aluminium holder to cover a small hole that had previously been drilled. The edges and any

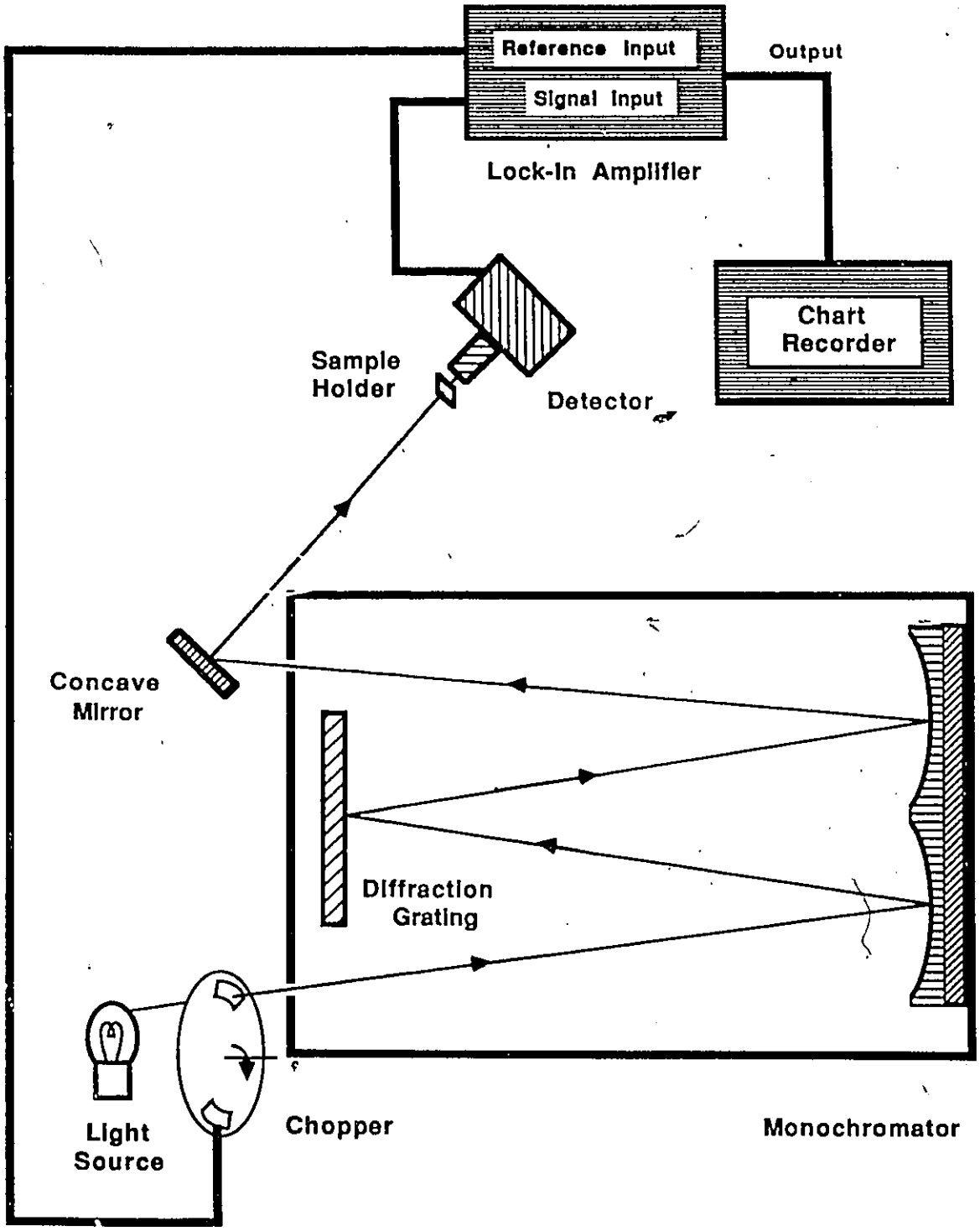

FIGURE 3.1 Schematic diagram of the optical absorption montage.

visible holes in the samples were blocked with silver print.

Measurements of I_O and I_T were then carried out as a function of wavelength in intervals of 1 - 2.5 nm near the absorption edge and in intervals of 5 - 10 nm beyond the absorption edge to permit the calculation of the background signal. The thickness d was measured after the experiment with a micrometer.

Figure 3.2a shows the graph of equation 3.4 which allows the absorption coefficient, α, to be determined as a function of hν, the photon energy for the sample 35/35/30. In this figure, the range of α which was measured was limited at the upper end by the signal to noise ratio (SNR) of the detection system and at the lower end by the background effects of the sample.

As can be seen in figure 3.2a, a typical value for $1/d*\ln (I_O/I_T)$ was of the order of 1400 cm^{-1} with the present system and a typical value for the background measurements was of the order of about 400 - 500 cm^{-1}. Despite this, the range of the absorption coefficient obtained was adequate to determine the energy band gap with sufficient accuracy, see figures 3.2b and 3.3.

The background effects can be attributed to various scattering centers such as impurity atoms, polycrystalline grains, or random arrangements of cations. They can also be attributed to free carrier effects or to impurities with lower energy band gaps.

Having obtained α as a function of photon energy, the energy gap for a direct transition is then determined from a graph of equation 3.1, using $n = 1/2$. Figure 3.3 shows the graph of $(\alpha h\nu)^2$ as a function of photon energy which allows E_g, the energy gap to be determined for the sample 35/35/30.

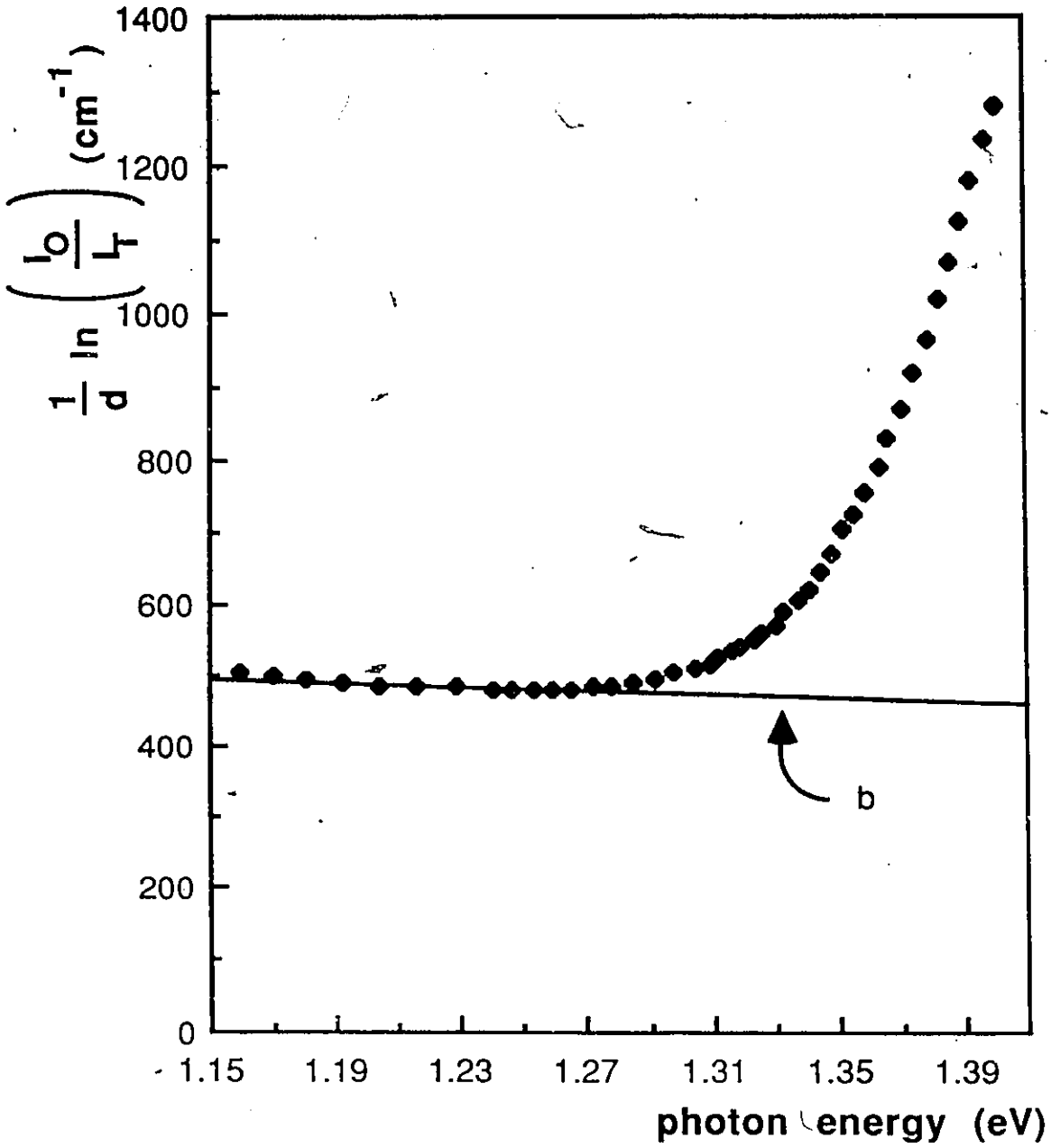

FIGURE 3.2a Graph of $1/d \ln (I_O/I_T)$ as a function of photon energy, hν for the sample 35/35/30. The absorption coefficient, α is calculated by subtracting b, the background signal + ln k from the curve.

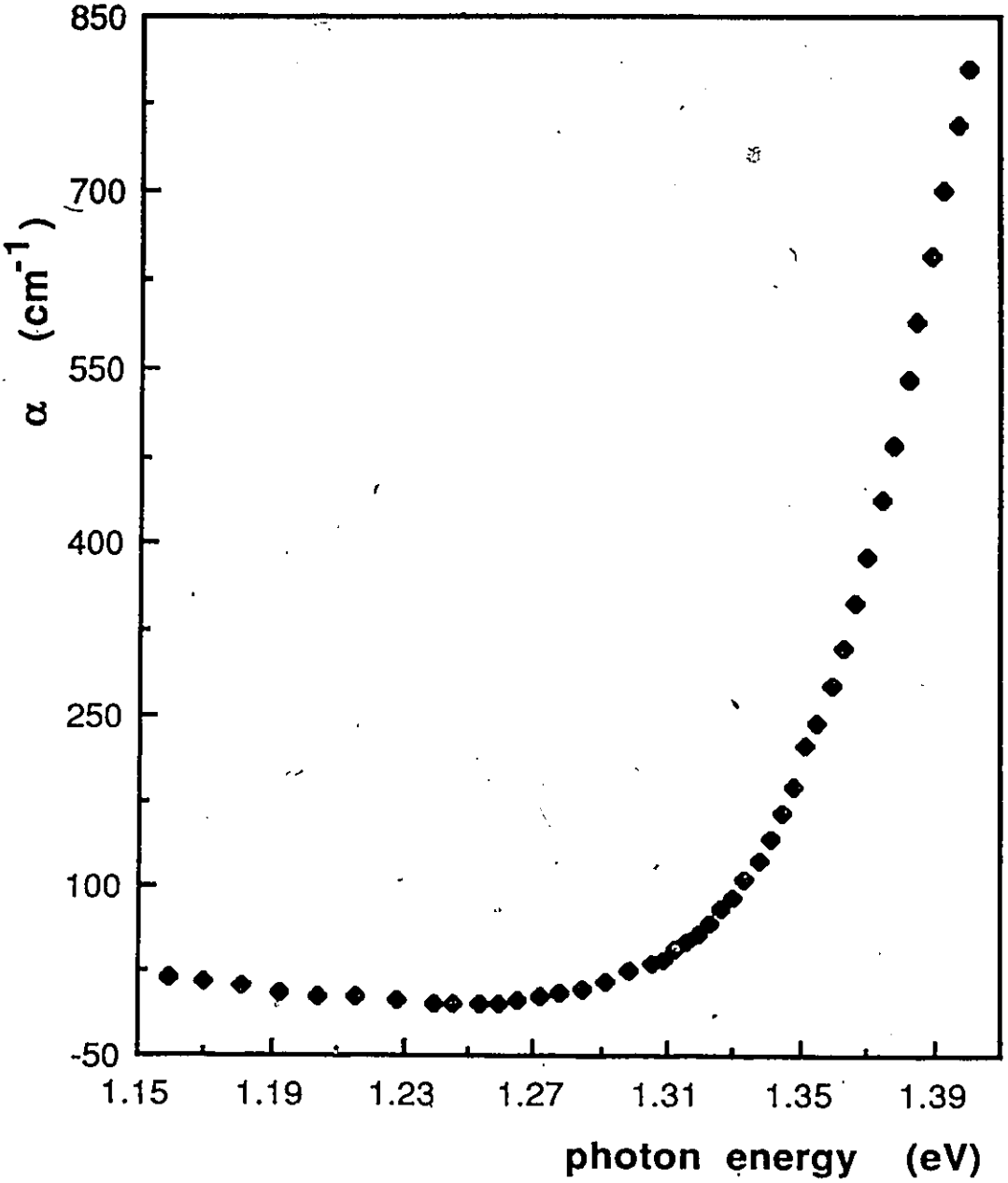

FIGURE 3.2b Graph of the absorption coefficient as a function of the photon energy for the sample 35/35/30.

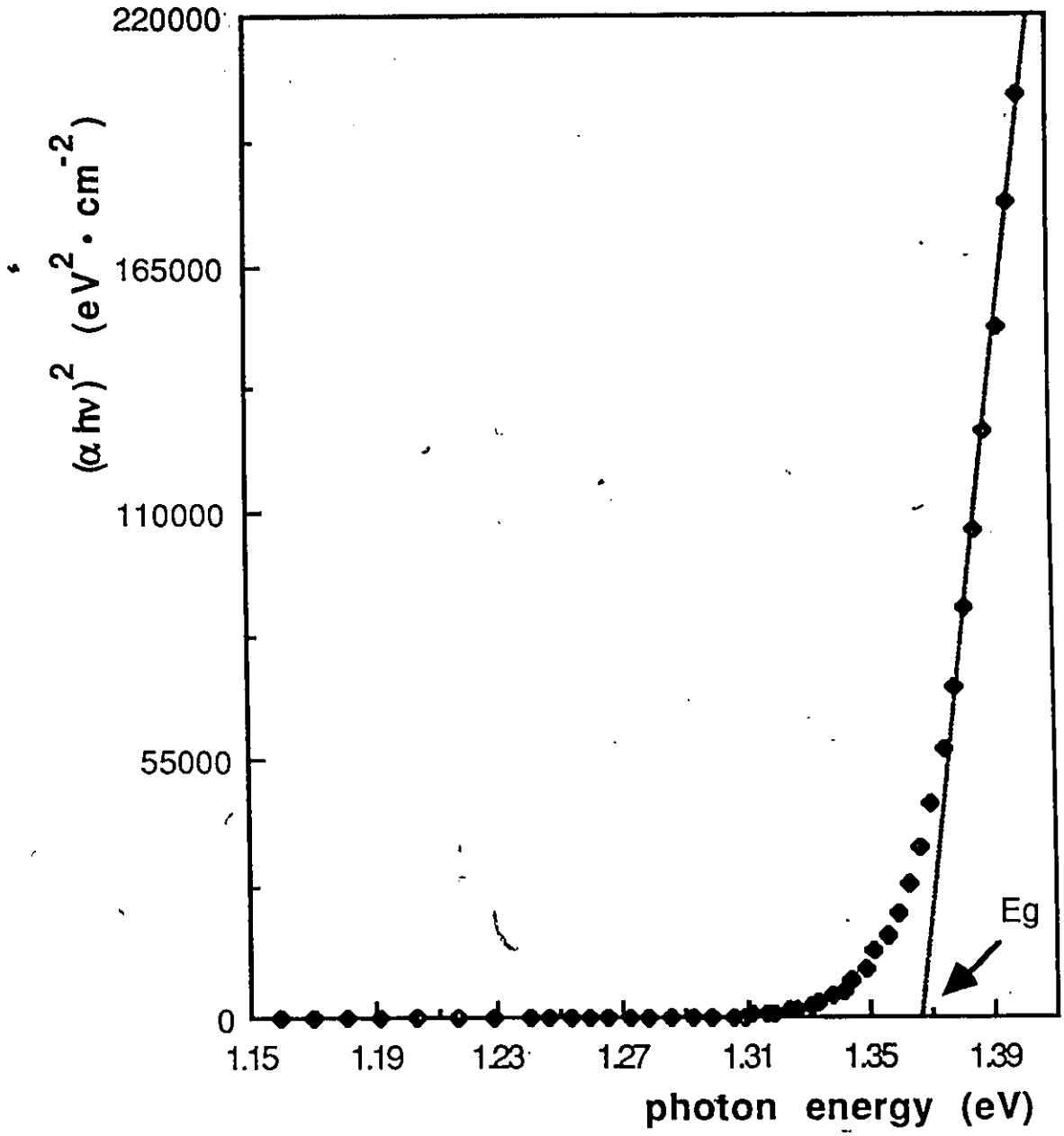

FIGURE 3.3 Graph of $(\alpha h\nu)^2$ as a function of photon energy, $h\nu$ for the sample 35/35/30. The linear extrapolation gives E_g, the energy gap.

3.4 Results and Discussion

Figure 3.4 and figure 3.5 show the energy gap values as a function of z and y concentration respectively for lines of constant f ratio. On these graphs, the lines of constant f ratio for the zinc blende and chalcopyrite structures extrapolate to points other than those for disordered structures which suggests that some type of ordering occurs in the zinc blende and chalcopyrite phases of this system. These ordered phases have also been observed in $Cd_{2x}(CuIn)_yMn_{2z}Te_2$ (86Q1), $Cd_{2x}(AgIn)_yMn_{2z}Te_2$ (85Q3), $Cd_{2x}(AgGa)_yMn_{2z}Te_2$ (87A1) and in $Zn_{2x}(CuIn)_yMn_{2z}Te_2$ (87N1), although the exact type of ordering has not been determined yet.

Neutron diffraction investigation, however, should give the type of ordered structure for these systems, but particularly for the $Zn_{2x}(CuIn)_yMn_{2z}Te_2$ system since it does not contain cadmium. Cadmium, because of its high neutron absorption impedes the scattering measurements in neutron diffraction. Investigations into this problem are presently being carried out at Chalk River by Daniel Bissonnette, another graduate student of the same semiconductor lab.

Returning to figure 3.4 and 3.5, the constant f ratio lines extrapolate to energy gap values in which the compound MnTe (z = 100 % in figure 3.4 and y = 0 % in figure 3.5) would have if it were in an ordered zinc blende structure (~1.9 eV) and in an ordered chalcopyrite structure (~1.35 eV). These extrapolated points are found to be consistent with the values previously obtained in the above systems (85Q3, 86Q1, 87A1, 87N1).

If lines are drawn to the extrapolated values for the disordered zinc blende and the disordered chalcopyrite structures determined from the above systems (~ 2.8 eV and ~ 2.25 eV respectively), then the boundaries between the ordered and

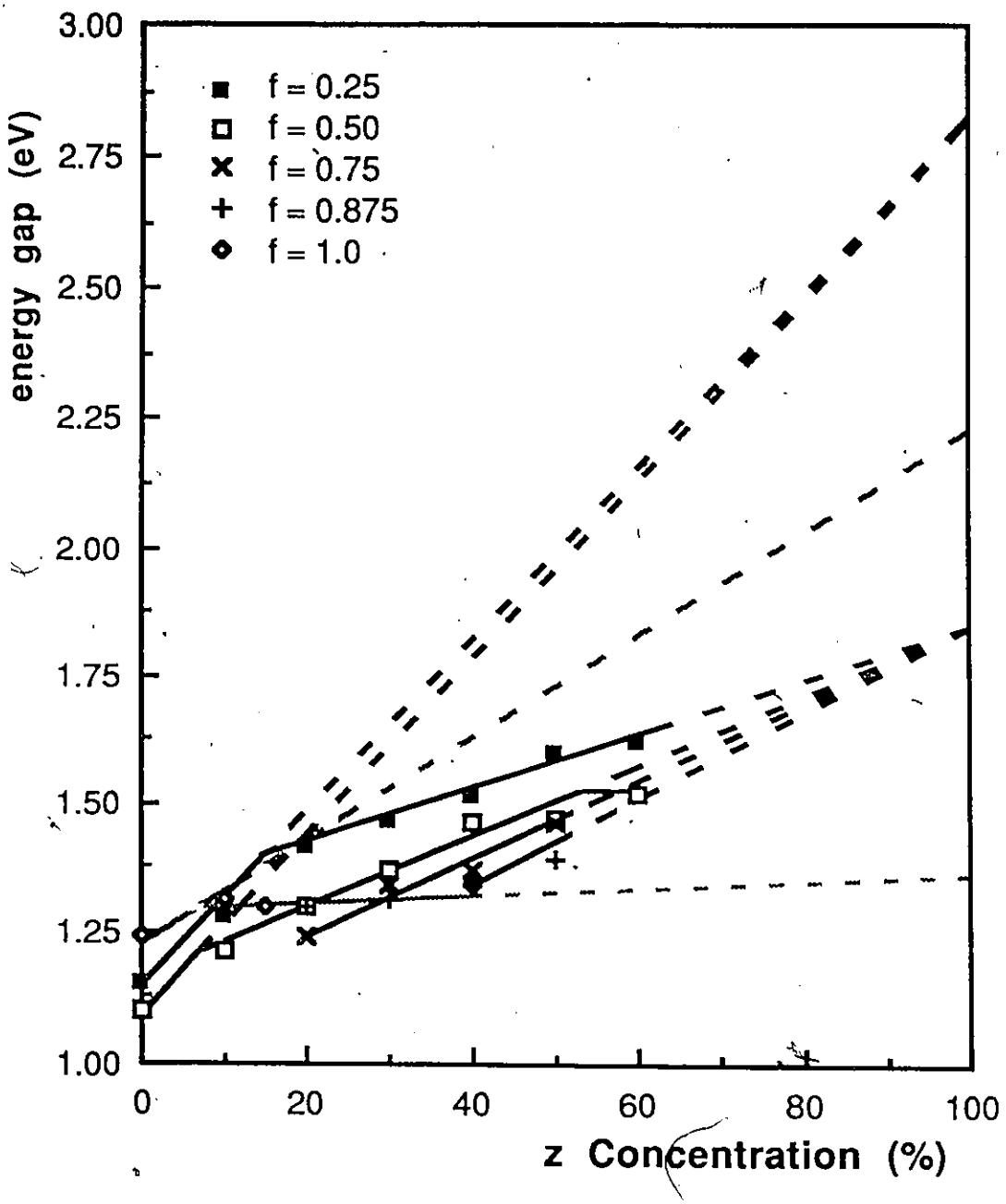

FIGURE 3.4 Variation of energy gap with z concentration. The black lines extrapolate to a hypothetical disordered and ordered structure while the gray lines extrapolate to a hypothetical disordered and ordered chalcopyrite structure for the MnTe compound.

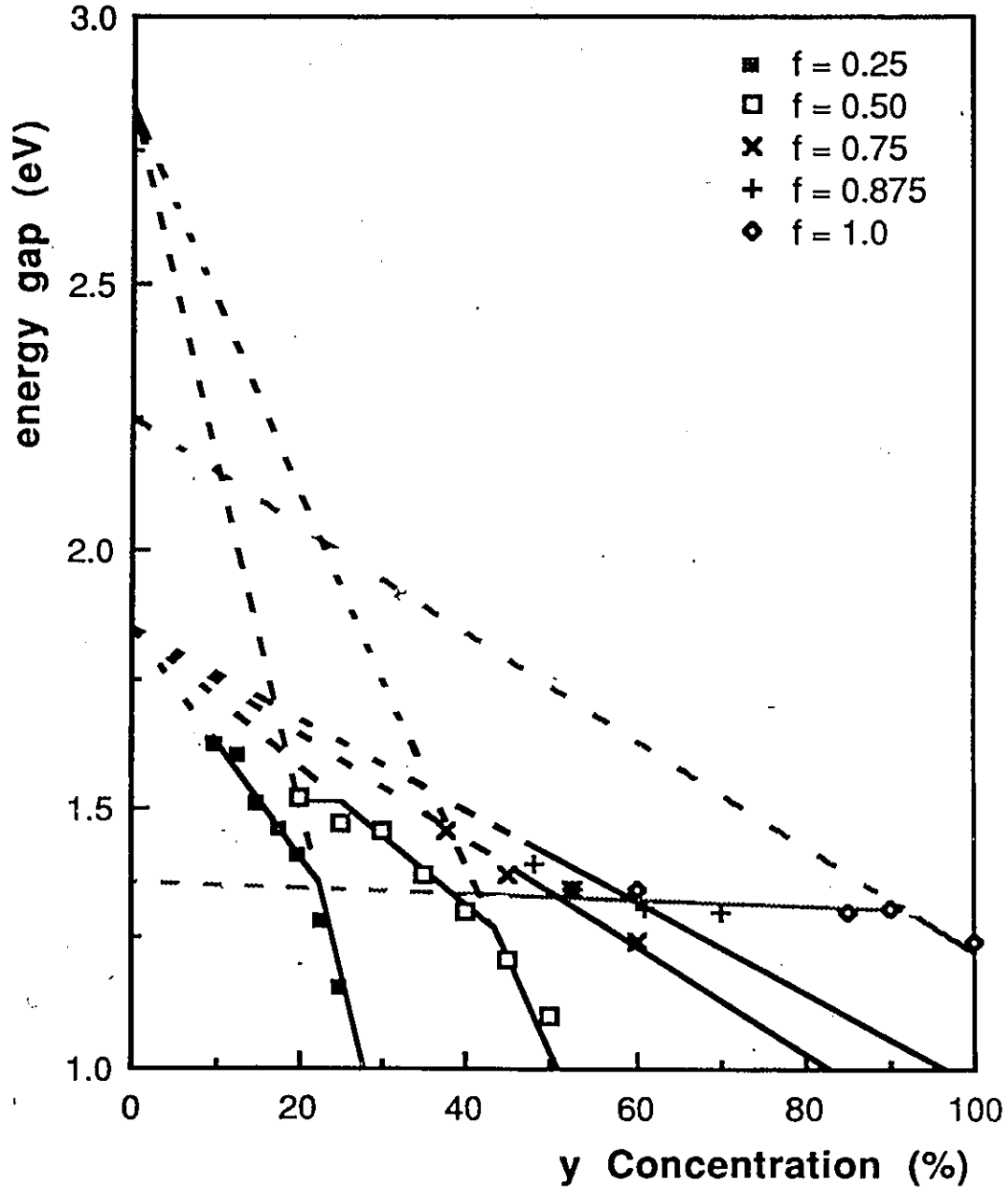

FIGURE 3.5 Variation of energy gap with z concentration. The black lines extrapolate to a hypothetical disordered and ordered structure while the gray lines extrapolate to a hypothetical disordered and ordered chalcopyrite structure for the MnTe compound.

disordered zinc blende and chalcopyrite phase fields can be determined from the points where changes of slope occur in the various lines.

These points where changes of slope occur have been used to give an approximate indication of the boundary of the ordered phases, see figure 3.7. In this figure, the ordered zinc blende phase is seen to cover most of the diagram, much as in the other alloy systems discussed above, ie. $Cd_{2x}(CuIn)_yMn_{2z}Te_2$ (86Q1), $Cd_{2x}(AgIn)_yMn_{2z}Te_2$ (85Q3), $Cd_{2x}(AgGa)_yMn_{2z}Te_2$ (87A1) and $Zn_{2x}(CuIn)_yMn_{2z}Te_2$ (87N1). However, more work is needed in order to delimit with more accuracy the ordered chalcopyrite and the (zb + ch) phase fields. Such work could be done by differential thermal analysis (DTA).

Figure 3.6 shows the variation of the energy gap with y concentration for lines of constant manganese concentration. From these curves, it is observed that the energy gap is reduced abruptly from y = 0 % to ~18 %. But this is due to the fact that the lattice undergoes a structural change, ie. the disordered zinc blende lattice becomes an ordered zinc blende lattice.

Now that the final form of the isothermal section has been obtained, the magnetic properties will be discussed starting with ESR analysis in chapter 4 and with magnetic susceptibility analysis in chapter 5.

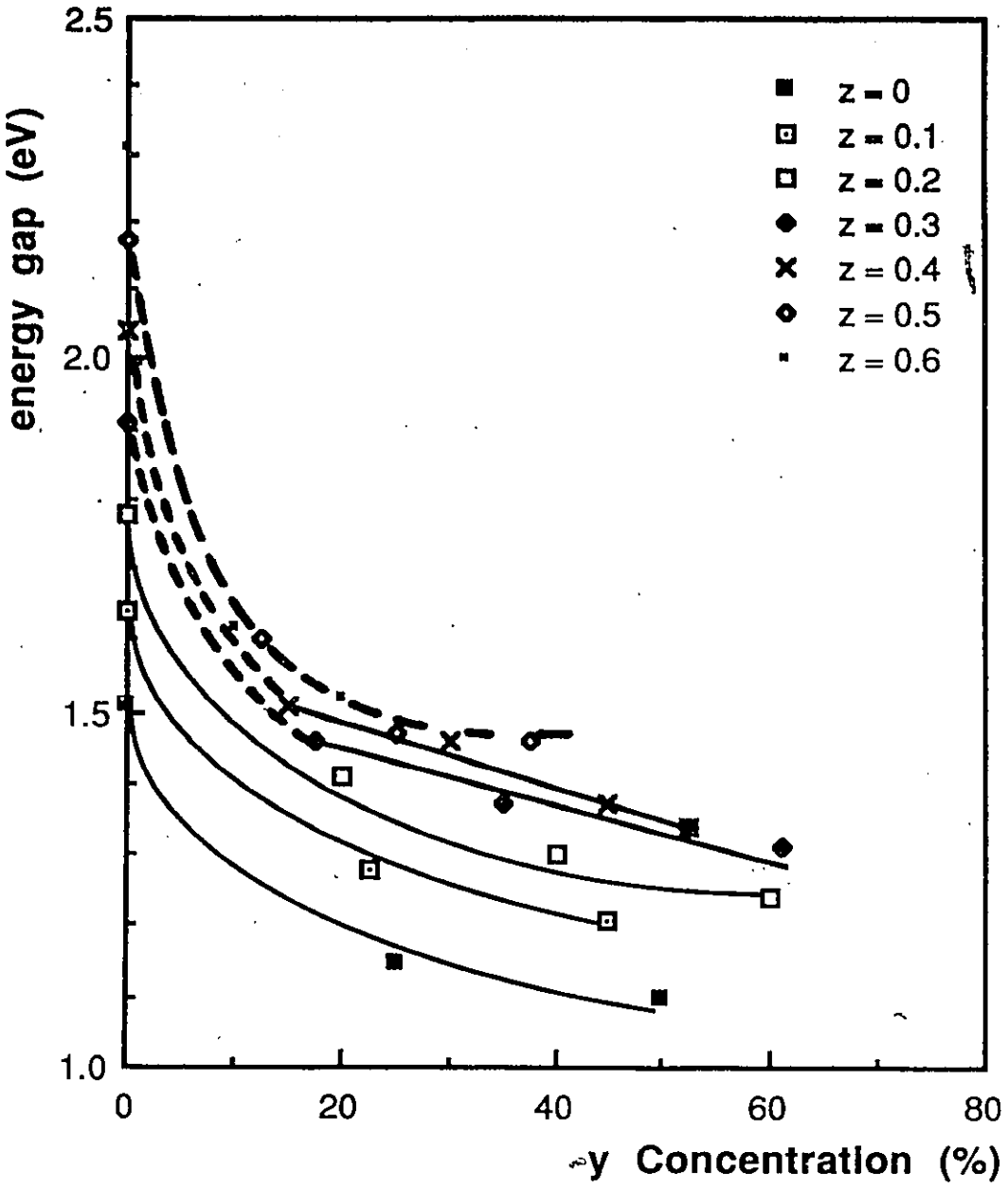

FIGURE 3.6 Variation of energy gap with y concentration for constant manganese concentration. The values at y=0 are taken from Donofrio et al. (86D1).

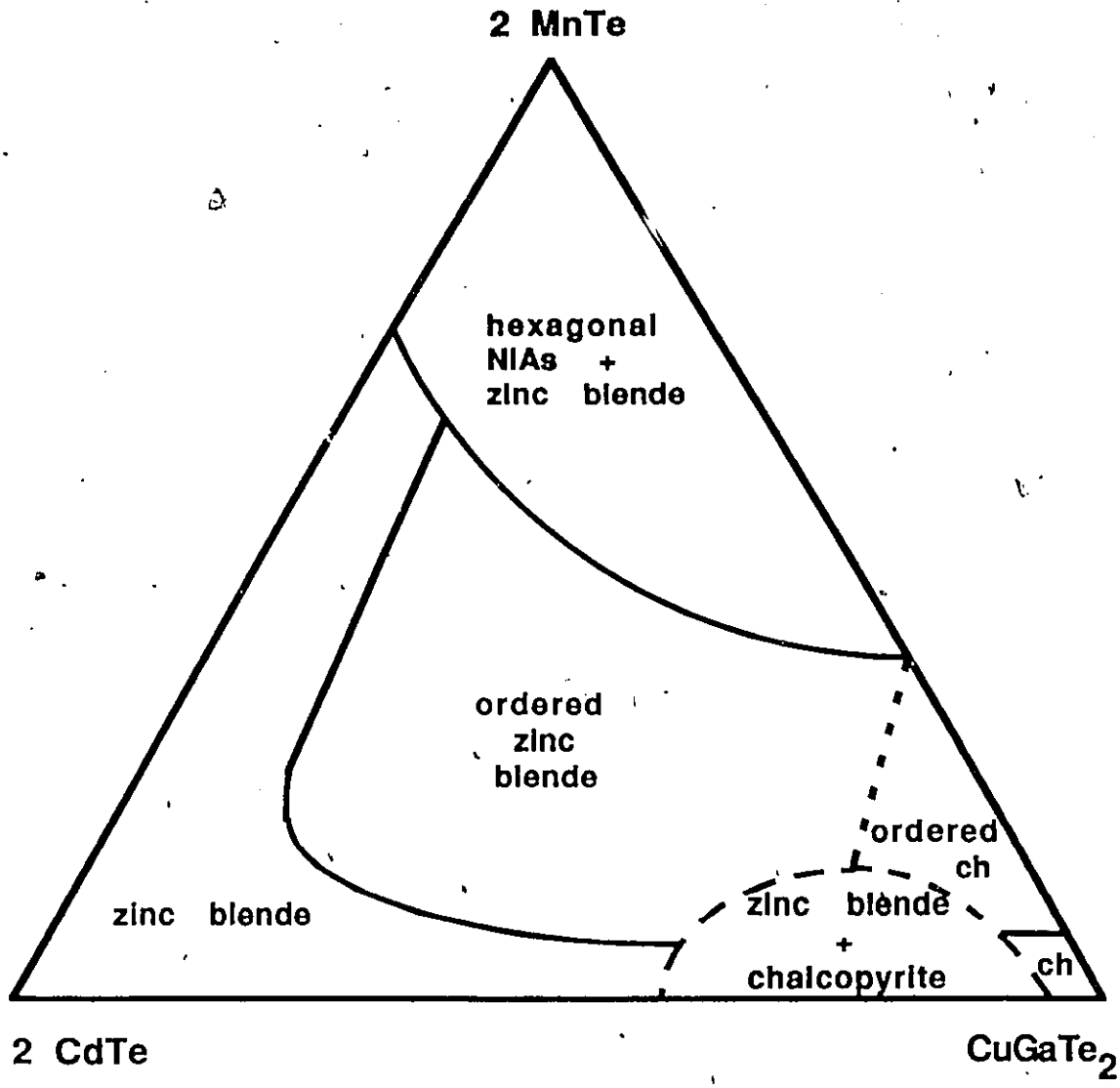

FIGURE 3.7 Estimated phase condition of the $Cd_{2x}(CuGa)_yMn_{2x}Te_2$ alloy system for T<550°C drawn from crystallographic analysis, differential thermal analysis (DTA) and optical absorption analysis.

CHAPTER 4 ELECTRON SPIN RESONANCE ANALYSIS

4.1 Introduction

Measurements of ESR linewidth ΔH as a function of temperature T have been made on single phase samples of the present system. Their purpose was to investigate the causes of broadening in linewidth as a function of temperature and composition. Webb et al. (84W1) and Sayad & Bhagat (85S1) suggested that in the disordered alloys, the main cause is spatial inhomogeneity. Webb et al. (84W1) showed that in that case the variation of ΔH can be represented by an empirical form of temperature dependence given by:

$$\Delta H = \Gamma \exp\left(-\frac{T}{T_o}\right) \qquad \text{(equation 4.1)}$$

Chehab et al. (86C1) and Woolley et al. (87W2) suggested that a paramagnetic contribution comes into effect at higher temperatures and should be added to ΔH. Therefore, the resultant relation of linewidth variation with temperature for the disordered alloys looks like:

$$\Delta H = \Gamma \exp\left(-\frac{T}{T_o}\right) + B\left\{1 - \exp\left(-\frac{T}{T_o}\right)\right\}\left(1 - \frac{\theta}{T}\right) \qquad \text{(equation 4.2)}$$

where Γ is proportional to the width of the distribution of the local field seen by manganese ions in the lattice.

T_o is proportional to the potential barrier separating two neighbouring ground

states of the disordered spin system.

B is the linewidth due to paramagnetic effects at high temperatures.

and θ is the Curie-Weiss paramagnetic temperature.

In this report, the results of linewidth, ΔH as a function of temperature are analysed in terms of equation 4.2 and the values of Γ, T_0 and B are determined by a least squares fit to the above equation.

4.2 Theory

According to atomic physics, the manganese ion, Mn^{2+} in the $Cd_{2x}(CuGa)_yMn_{2z}Te_2$ alloy system, has a total angular momentum quantum number, J which is associated with a net magnetic moment. It is this net magnetic moment which is responsible for the magnetic properties in these SMSC's. In Mn^{2+} the total angular momentum quantum number, J is equal to S, the total spin angular momentum quantum number because the total orbital momentum quantum number is quenched, ie. $L = 0$.

Also, according to atomic physics, a free ion which possesses a total angular momentum quantum number, J has $2J + 1$ degenerate levels which may be split by the application of a magnetic field H, see figure 4.1(a) for the case of manganese. This is known as the Zeeman effect. The energies of these degenerate levels are described by:

$$E = g\ \mu_B\ M_J\ H \qquad \text{(equation 4.3)}$$

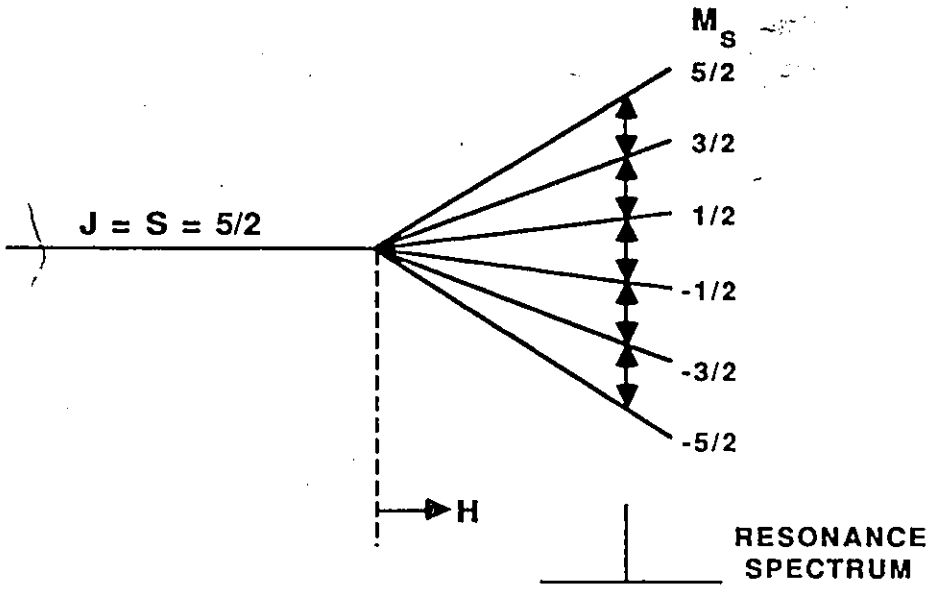

FIGURE 4.1(a) Zeeman Splitting of a $3d^5$ level. In this example there is only one resonance line.

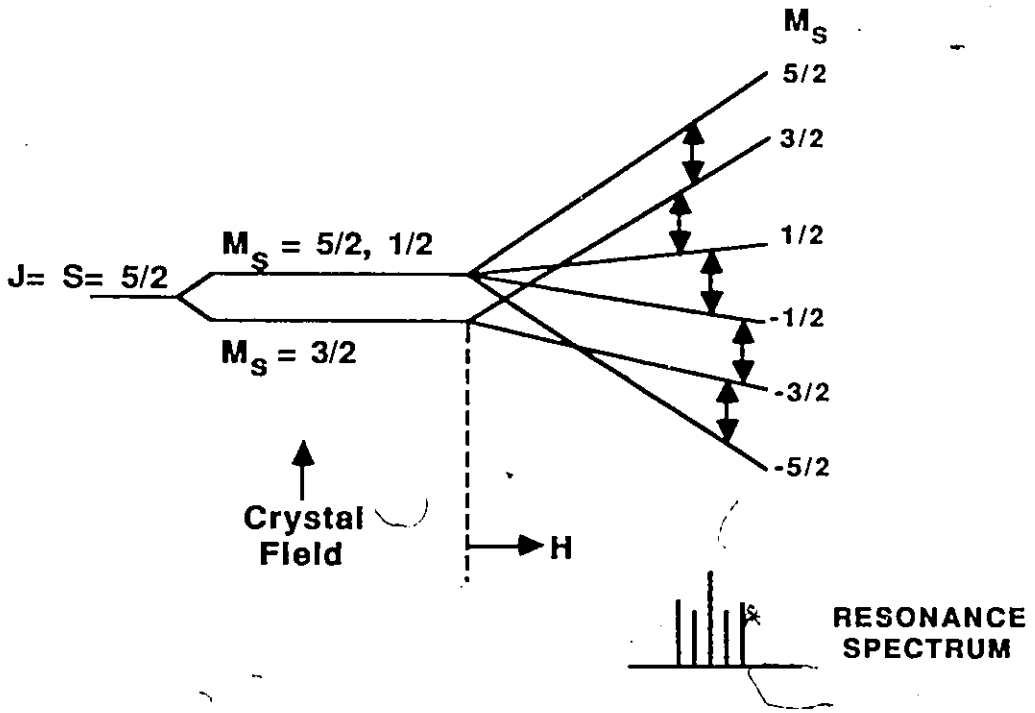

FIGURE 4.1(b) Energy level diagram of a $3d^5$ level in an octahedral crystal field. The single resonance line is split into five by the presence of a crystal field.

where g is the gyromagnetic factor.

μ_B is the Bohr magneton.

M_J (= -5/2, -3/2, -1/2, 1/2, 3/2, 5/2 for Mn^{2+}) is the magnetic quantum number.

and H is the magnetic field applied.

In Electron Spin Resonance, transitions between these energy levels are induced by an electromagnetic radiation of angular frequency ω, in the presence of a magnetic field. In the lab, the resonance is observed by fixing ω in the microwave range and by varying the magnetic field, H. According to quantum mechanics, the selection rules are such that only transitions between adjacent levels are allowed so that for the free manganese ion in figure 4.1(a), only a single resonance line will be observed, given by:

$$\Delta E = g \mu_B H = \hbar \omega \qquad \text{(equation 4.4)}$$

where ω is the angular frequency.

and $\hbar$ is Planck's constant.

In SMSC alloys, however, the manganese ion cannot be treated as an isolated free ion and hence perturbing external effects must be considered. For example, in the presence of an octahedral crystal field, the single resonance line of figure 4.1(a) splits into five lines, see figure 4.1(b). Other effects such as the hyperfine coupling have also been shown to split the resonance spectrum of the manganese ion into six sets of quintets (72W1).

Experimentally, however, the resonance spectrum of these SMSC alloys does

not occur at a sharply defined magnetic field. Instead it is spread out over a range of H. The size of the spread depends on relaxation phenomena, such as spin-spin and exchange interactions. It also depends on inhomogeneous broadening which is caused by an overlapping of any hyperfine structure, as well as by the presence of inhomogeneous fields in the crystal.

In other words, inhomogeneous broadening occurs when the static or the time averaged magnetic field seen by each magnetic dipole moment or spin in the crystal is not the same. This results in a superposition of a large number of individual components, or spin packets, each slightly shifted from the others in the resonance line with a resultant envelope of an approximate gaussian shape.

In the present materials, the inhomogeneous effects are much larger than the relaxation effects and so the relaxation effects can be neglected (87W2). Thus, for disordered alloys, the empirical relationship between ESR linewidth and temperature must take a form which takes into account inhomogeneous broadening, ie. equation 4.2:

$$\Delta H = \Gamma \exp\left(-\frac{T}{T_o}\right) + B\left\{1 - \exp\left(-\frac{T}{T_o}\right)\right\}\left(1 - \frac{\theta}{T}\right) \qquad \text{(equation 4.2)}$$

In this equation, the first term is due to inhomogeneous broadening and the second term is due to a paramagnetic effect which becomes significant at high temperatures.

Using the experimental data of ΔH and T, and using the experimental value of the Curie-Weiss temperature, θ obtained from magnetic susceptibility measurements (chapter 5), the values of Γ, T_o and B are calculated by a least squares fit to

equation 4.2.

The values of T_o obtained are plotted as a function of z concentration since these values are expected to vary linearly with manganese concentration. This is because T_o is proportional to the potential barrier separating two neighbouring ground states of the disordered spin system.

The values of B obtained are also plotted as a function of z concentration since these values are also expected to vary linearly with manganese concentration. This is because B which is the linewidth due to paramagnetic effects at high temperatures is expected to be a function of the manganese concentration.

However, the values of Γ obtained in this analysis are found to vary non-linearly with z. This is to be expected because Γ is proportional to the width of the distribution of the local field seen by a Mn ion in the lattice. Since the relative width of any random arrangement is proportional to z(1-z) and since the total number in the distribution is proportional to the number of Mn atoms in the system; the actual width might be expected to be proportional to z^2 (1-z), ie. Γ should vary as $\Gamma = D\ z^2\ (1-z)$ (87W2).

4.3 Experiment

The resonance absorption for different compositions was observed over a wide temperature range (10 - 500 K). The actual measurements were performed by Bei Wah Chan of the ESR lab. Since the responsibility for the instruments rested in his hands, the apparatus will be described briefly.

The apparatus consisted of a microwave source, which supplied radiation at X-band frequency, about 9.4 GHz, and a waveguide system, which directed the waves into and out of a resonant cavity. Samples placed in the cavity would absorb the radiation when the resonance condition, equation 4.4, was satisfied. This was detected as a reduction in the intensity of the microwaves leaving the cavity. An electromagnet supplied the constant field which was applied to the resonant cavity. The field intensity could be adjusted from zero to about seven kilogauss, allowing for a maximum linewidth measurement of about 5.5 kgauss. Determining the width of a broad absorption line is simplified by measuring its derivative, so the static field was modulated by a small oscillating field. The linewidth was taken as the peak to peak distance of this derivative curve.

The experimental values of the linewidth, ΔH as a function of T, the temperature are plotted in figures 4.2 to 4.5 for the lines f = 0.25, f = 0.50, f = 0.75 and y = 0.50. Figure 4.6 gives the values of linewidth ΔH as a function temperature for different f ratio, but for constant Mn^{2+} concentration.

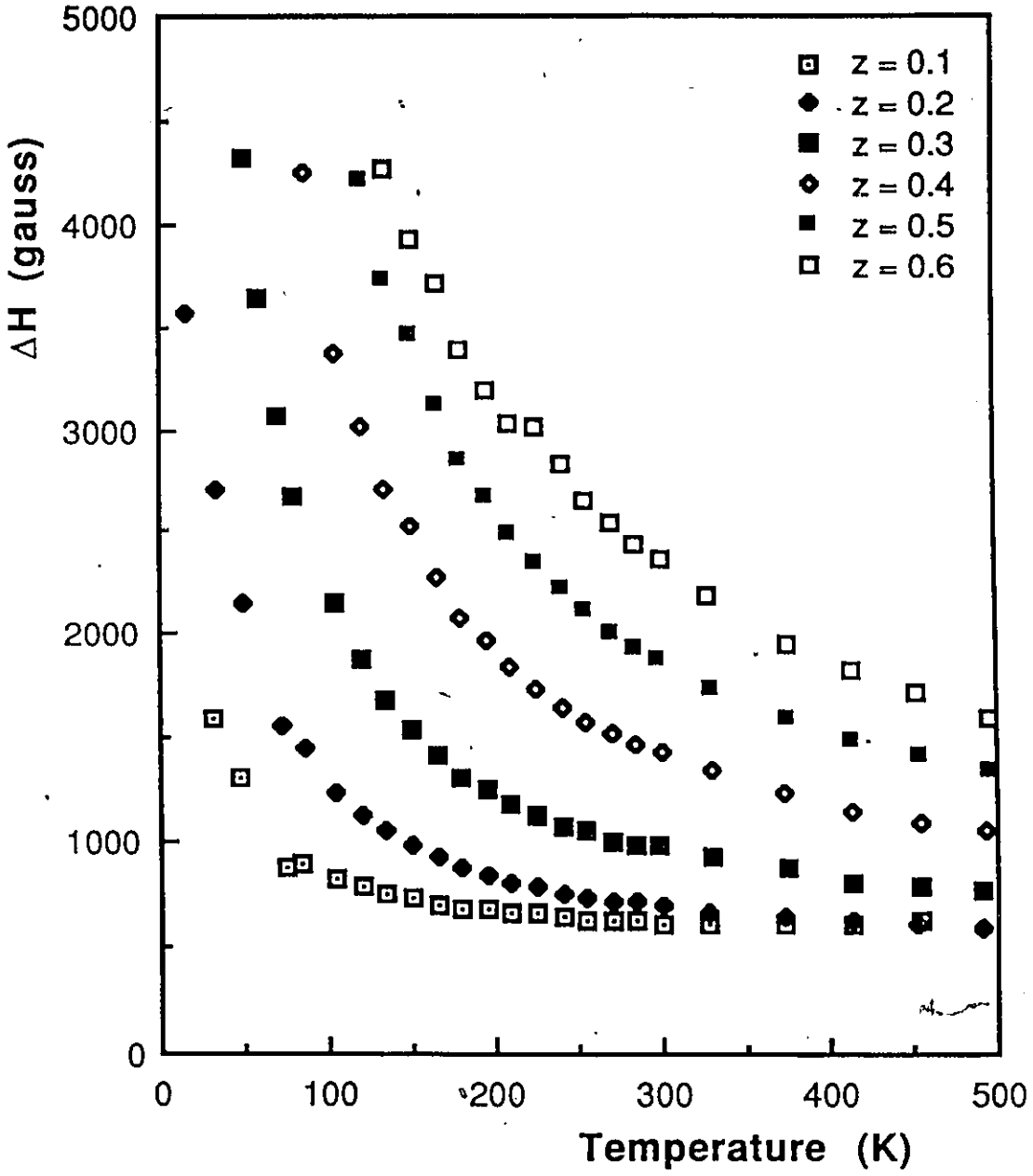

FIGURE 4.2 ESR linewidth as a function of temperature for f = 0.25.

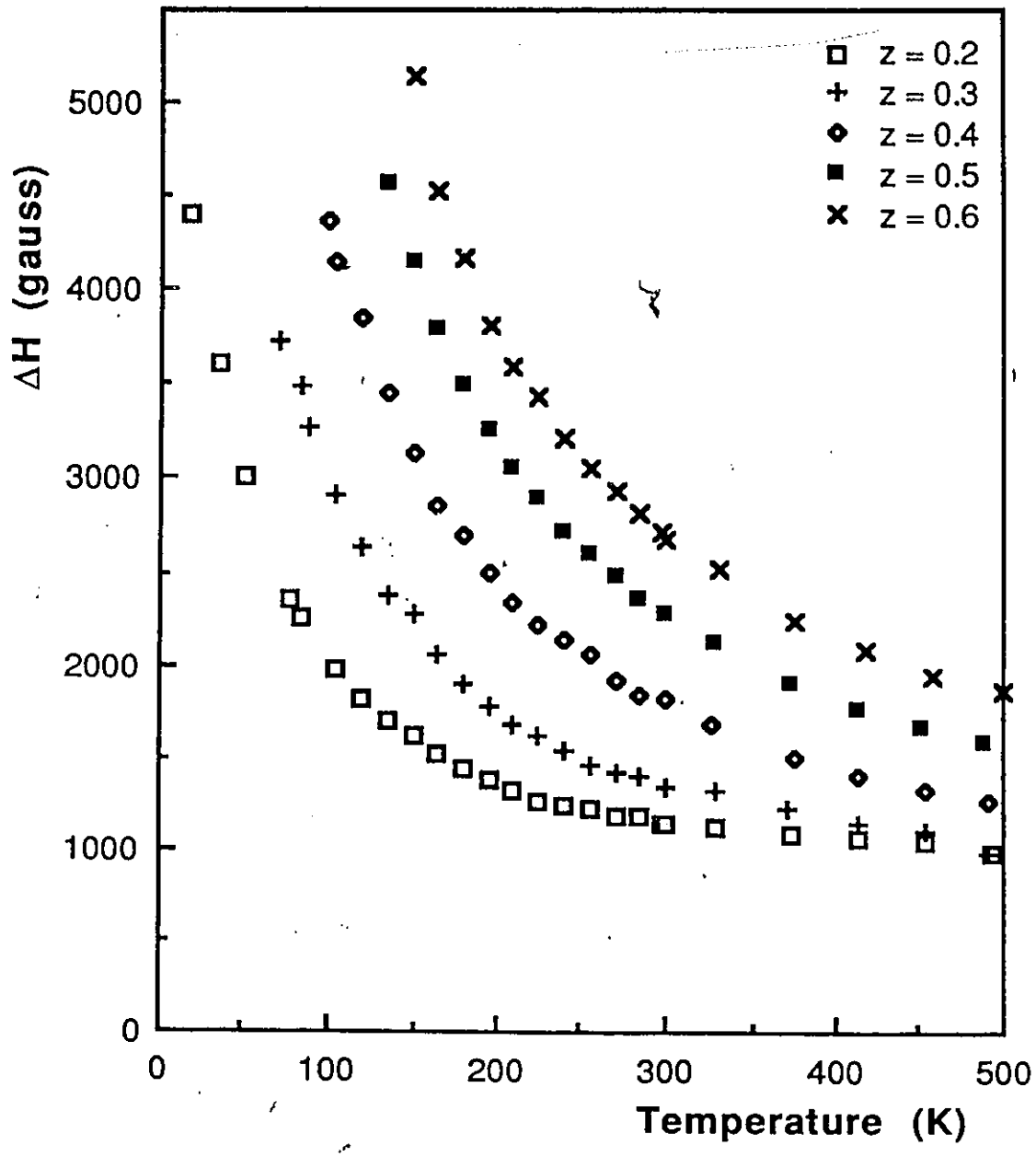

FIGURE 4.3 ESR linewidth as a function of temperature for f = 0.50.

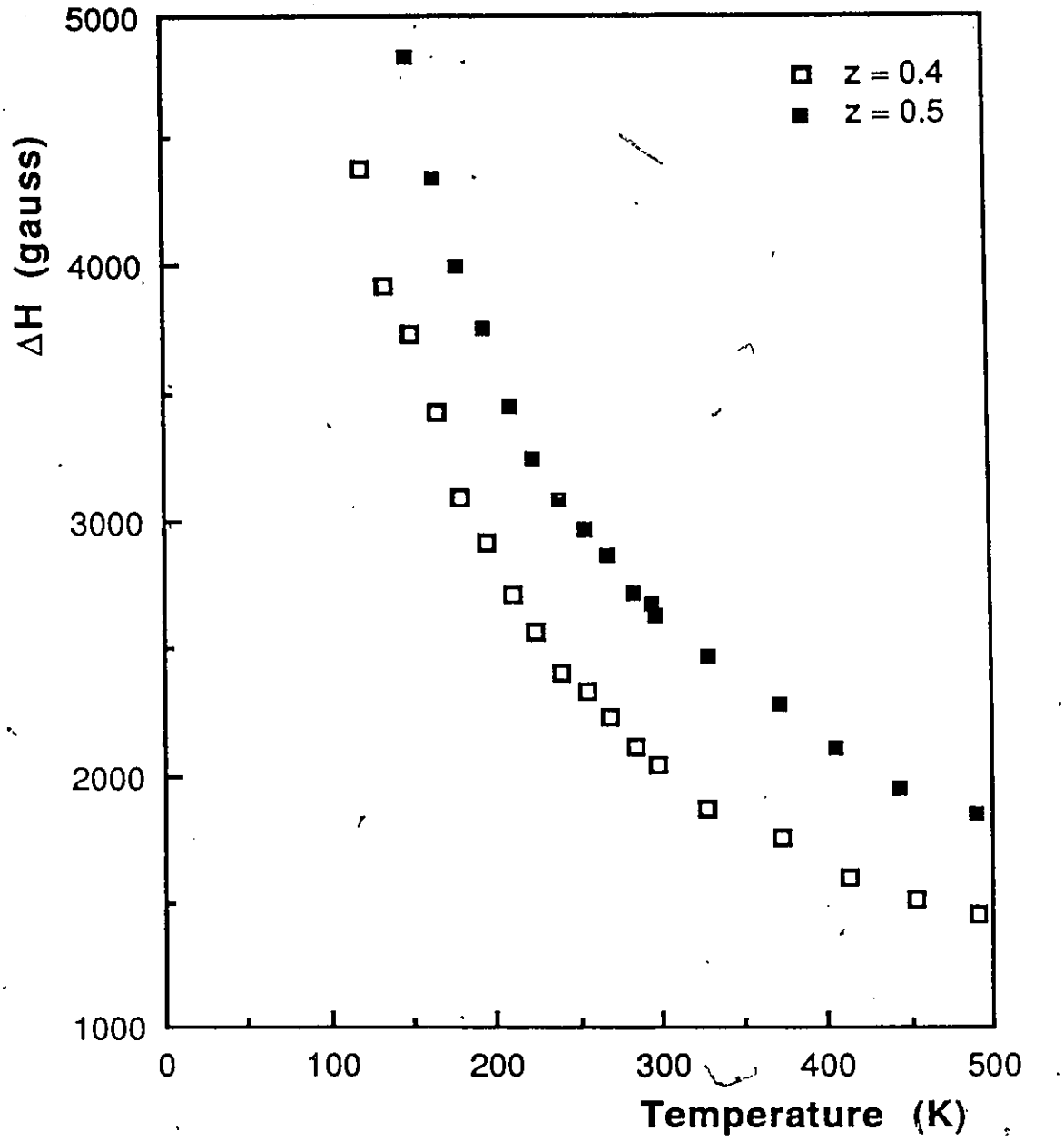

FIGURE 4.4 ESR linewidth as a function of temperature for f = 0.75.

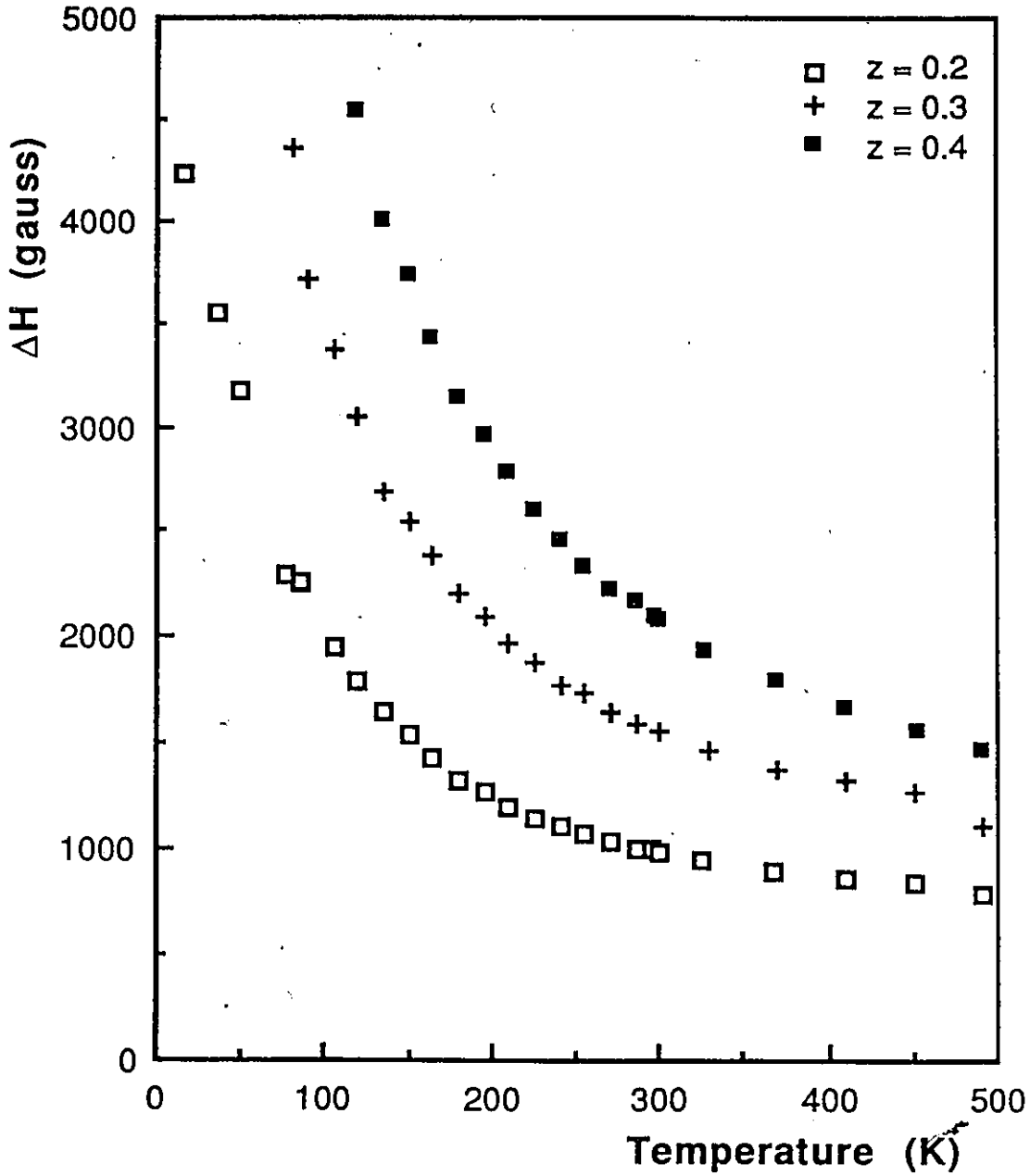

FIGURE 4.5 ESR linewidth as a function of temperature for $y = 0.50$.

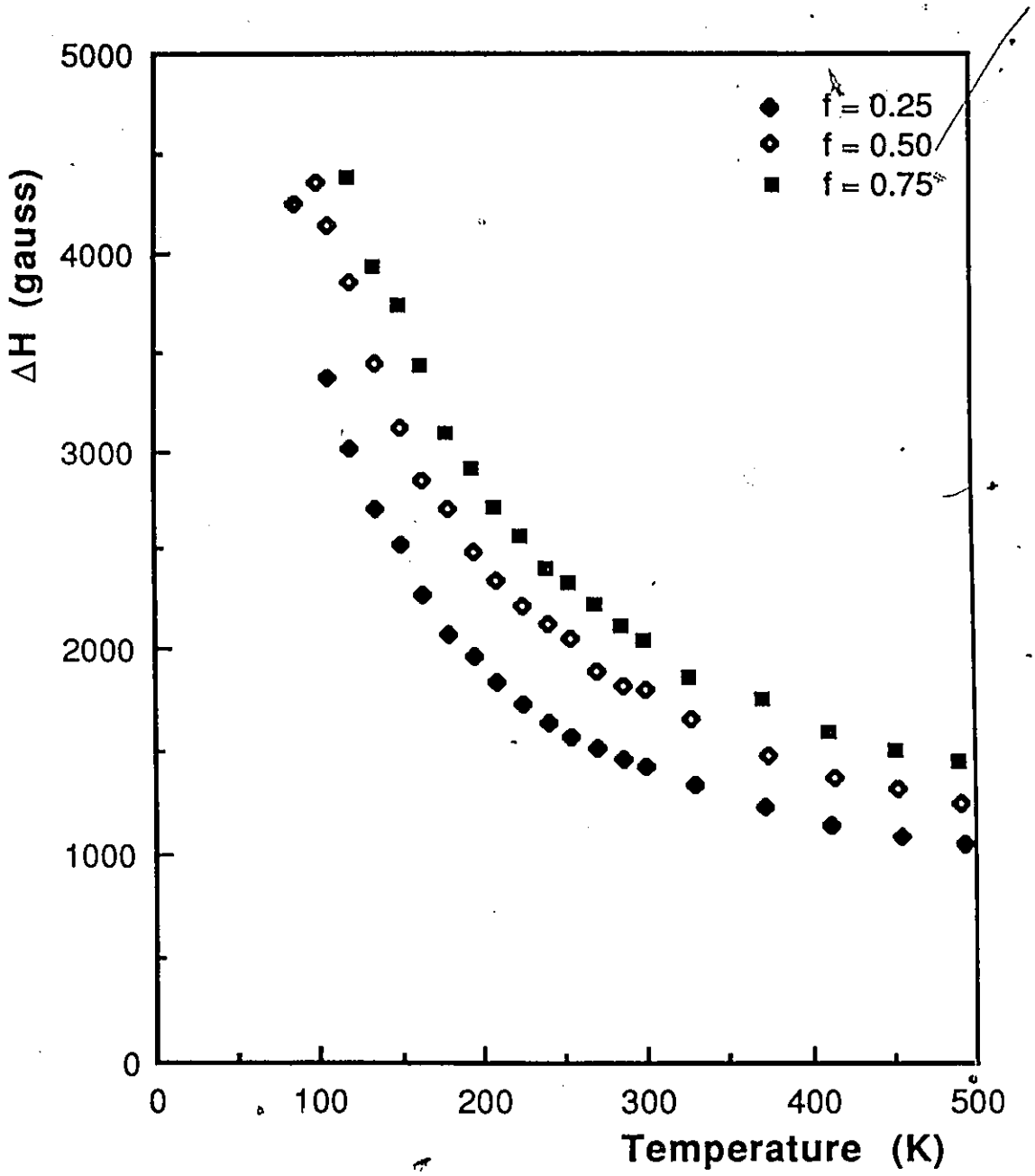

FIGURE 4.6 ESR linewidth as a function of temperature for $z = 0.40$.

4.4 Results and Discussion

From figures 4.2 to 4.5, the general observation that can be made is that the magnitude of the linewidth, ΔH increases with z, the manganese concentration. But this is to be expected since the manganese ion is solely responsible for the magnetic effect.

Figure 4.6 gives the values of linewidth ΔH as a function of temperature for different f ratios, but with constant Mn^{2+} concentration. From this figure, it can be seen that the linewidth is proportional to the f = y / x+y ratio. That is, as f increases, the linewidth is seen to increase also. But this is to be expected since from figure 2.5, the lattice parameter decreases for increasing f. This means that the many inhomogeneous fields which are responsible for inhomogeneous broadening are closer together as f increases, and hence contribute more.

Figure 4.7 and figure 4.8 respectively illustrate the variation of B, the linewidth due to paramagnetic effects at high temperatures and the variation of T_o, the potential barrier separating two neighbouring ground states of the disordered spin system, as a function of manganese concentration. From figures 4.7 and 4.8, those parameters are seen to vary linearly with manganese concentration as is to be expected.

Figure 4.9 shows the variation of Γ as a function of z^2 (1-z). Woolley et al. (87W2) mentions that the slope of that graph appears to be characteristic of the crystal structure involved. A value of ~56 kgauss is given for the zinc blende structure for their three systems analysed. The value obtained for the zinc blende structure of this system is ~73 kgauss which is close to that of Woolley et al. considering the smaller number of points used and the experimental scatter seen in figure 4.9.

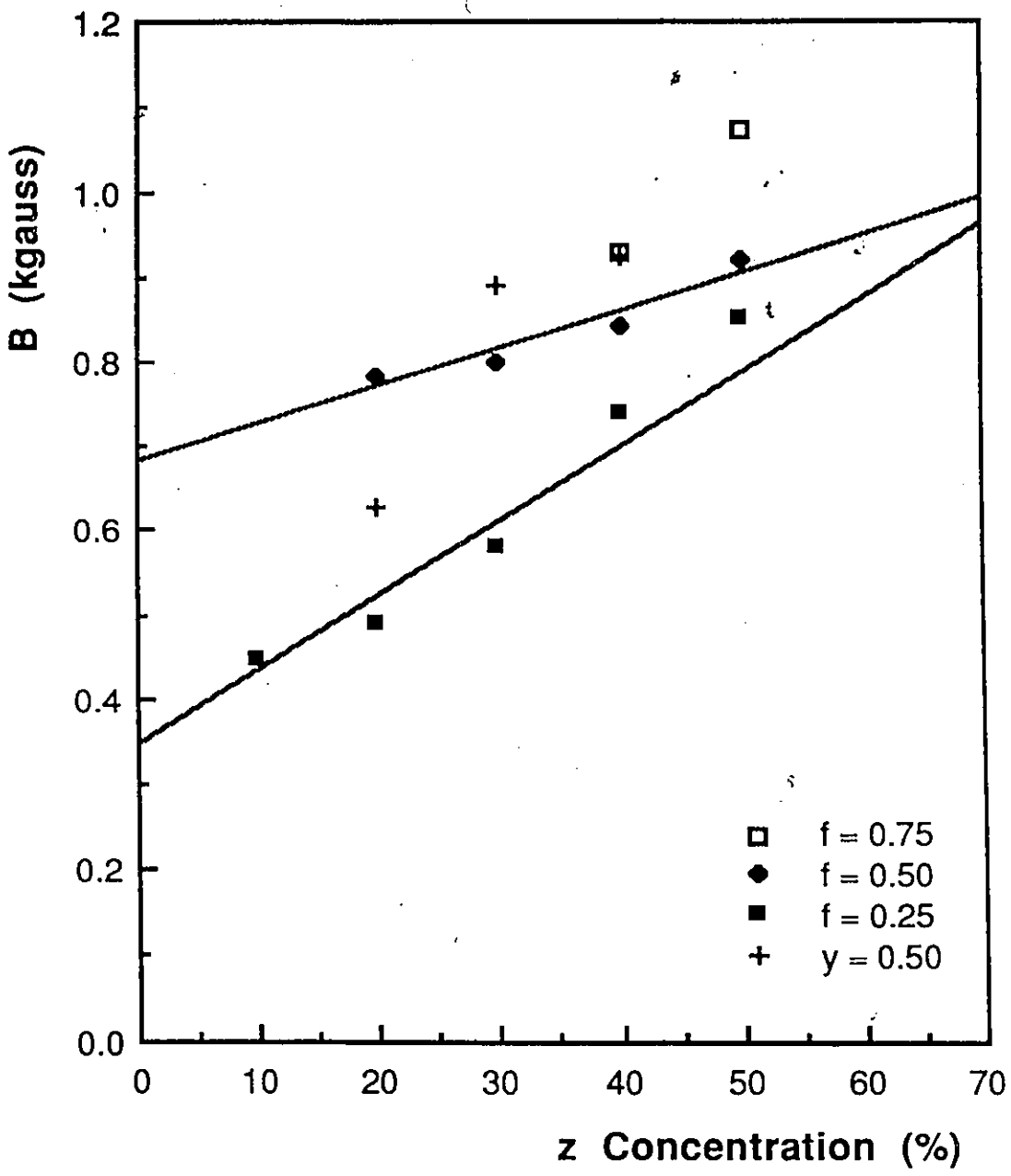

FIGURE 4.7 Linewidth B which is due to paramagnetic effects at high temperatures as a function of z concentration. The lines shown are fitted to the values of B for f=0.50 and f=0.25. Unfortunately, the other values of B have too much scatter to be fitted.

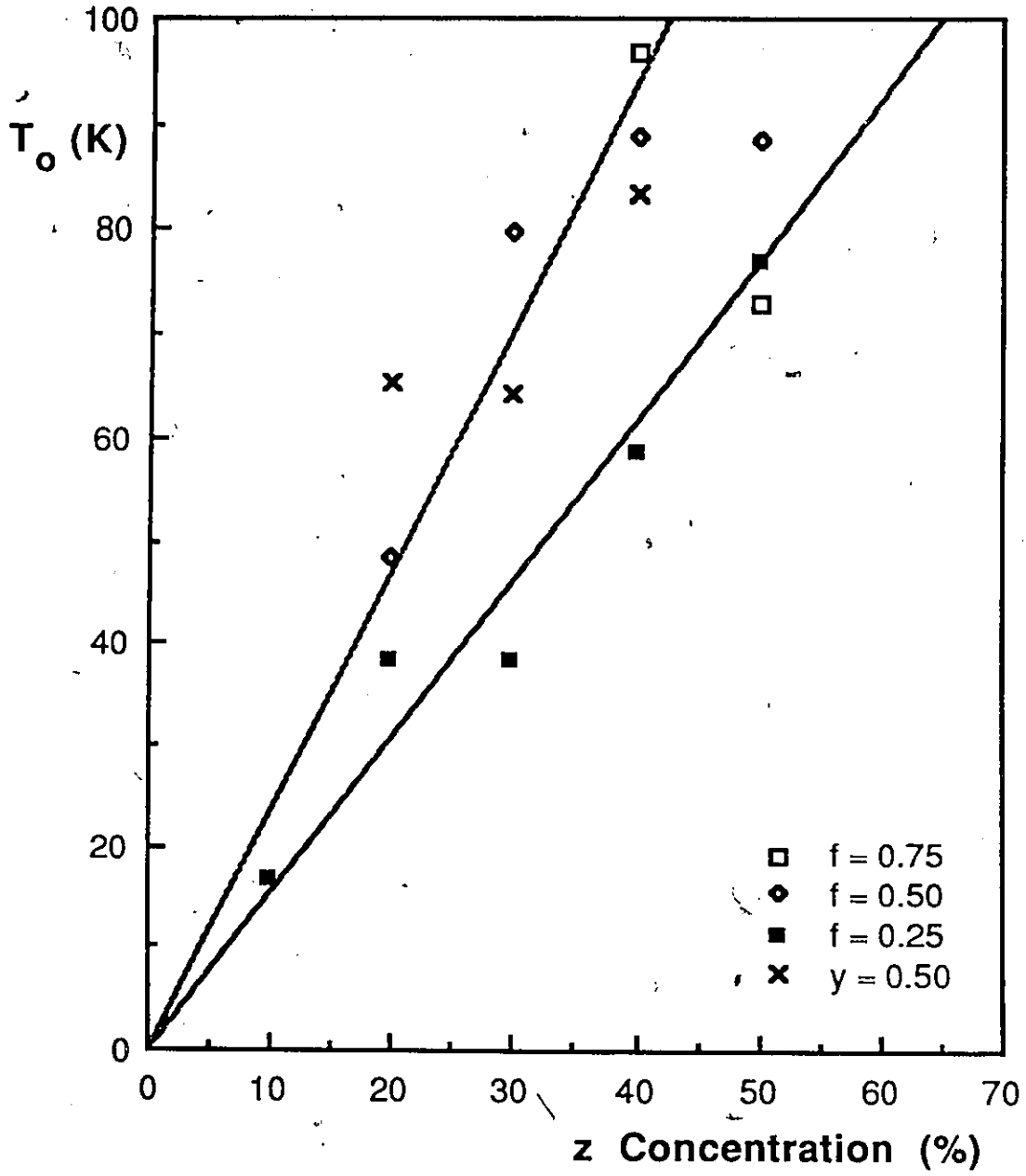

FIGURE 4.8 Variation of T_o as a function of z concentration. The lines are fitted to f=0.50 and to f=0.25.

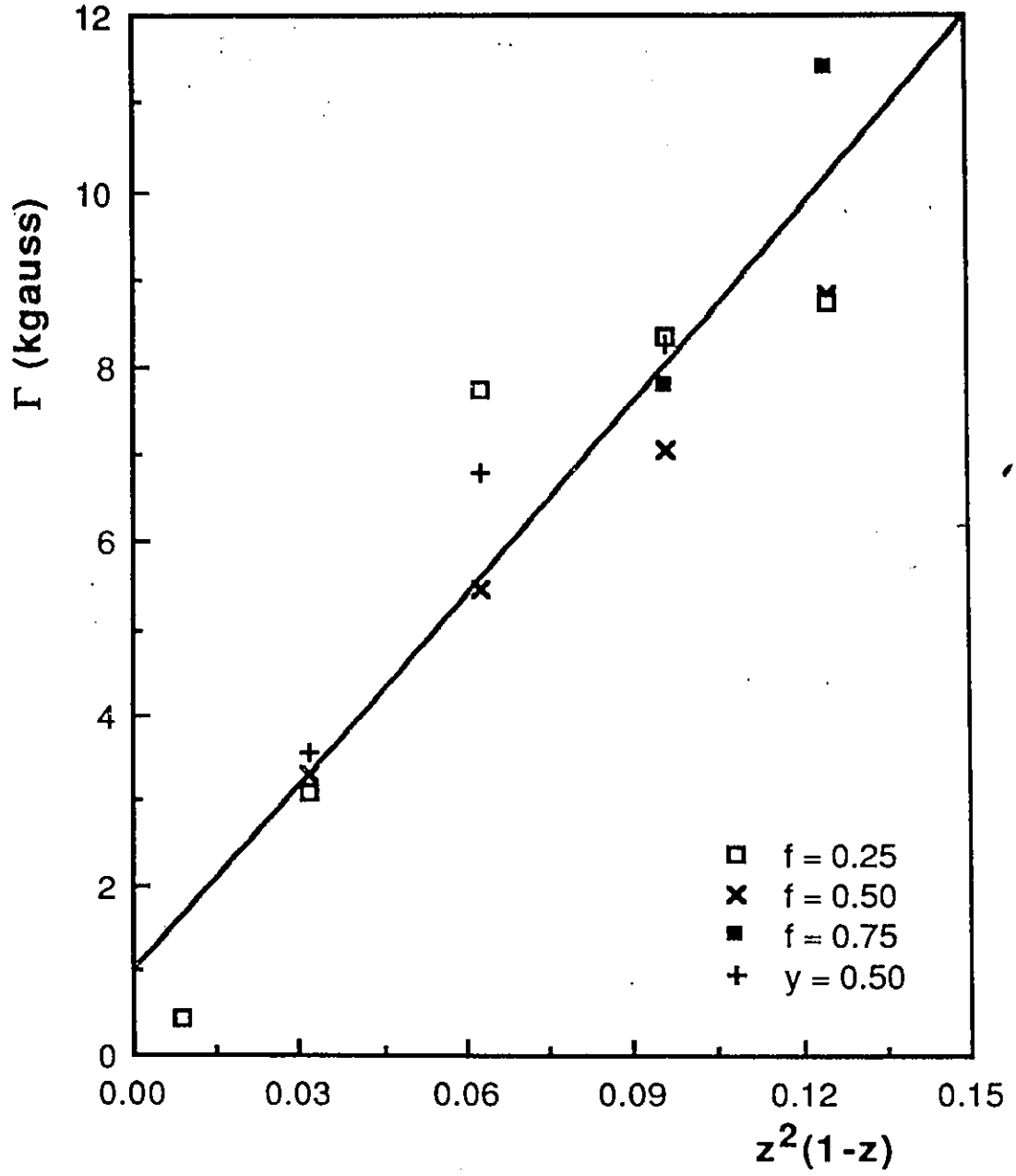

FIGURE 4.9 Linear variation of Γ with $z^2(1-z)$.

Some anomalies were encountered during the measurement of linewidth ΔH for some samples of this system. A first anomaly was that the samples with high f ratio, ie. f = 0.875 and f = 1.0 all displayed an asymmetric linewidth ΔH as a function of temperature. The result is that these linewidths could not be measured and no further analysis was possible for these samples. It is thought that an anisotropic crystal field which forms near the chalcopyrite phase field may be responsible for the asymmetry. This is still under investigation at the University of Ottawa.

Another anomaly encountered during the measurements of linewidth ΔH as a function of temperature is the presence of an extra linewidth ΔH_o, where $\Delta H_o \ll \Delta H$ with every sample of the system. It is thought that this ordered linewidth is due to the presence of an ordered zinc blende phase in the sample which can be eliminated from a disordered zinc blende phase depending on the annealing temperature during the preparation. Attempts are presently under way in the semiconductor lab to try to control the relative amounts of ordered and disordered phases present in samples. Again, this phenomenon is still under investigation at the University of Ottawa.

CHAPTER 5 MAGNETIC SUSCEPTIBILITY ANALYSIS

5.1 Introduction

Measurements of magnetic susceptibility in the range 4 - 250 K were made to give values of T_g, the spin-glass transition temperature and θ, the Curie-Weiss temperature. Because the values of T_g and θ depend on the concentration of the manganese ion present, the experimental values of T_g and θ obtained are plotted as a function of z, the manganese concentration for various f ratios. The significance of these parameters will be explained later.

By equating kT_g, the thermal energy at the spin-glass transition to the superexchange interaction energy proposed by Geertsma et al. (77G1), the appropriate parameters of the exchange mechanism are determined. These values are compared to other results obtained from other similar SMSC systems (87M1).

Values of the Curie-Weiss temperature, θ may also be calculated by using the mean field theory and the superexchange parameter calculated above. These values are then fitted by a least squares method and the resulting line obtained is compared to the experimental values of θ.

5.2 Background

A spin glass is a 'freezing' of spins into random orientations. This freezing is accompanied by a cusp in the magnetic susceptibility measurements made as a function of temperature. However, no corresponding anomaly is observed in the specific heat (82G2). In semimagnetic semiconductors (SMSC's), the random

orientation of the spin glass is due to a lattice induced 'frustration' of the antiferromagnetic interaction (84B1). This frustration results from the competing influences of two neighbouring spins of opposite direction. This situation is depicted in figure 5.1.

In SMSC's, the resultant antiferromagnetic interaction between spins is a consequence of different exchange interactions (80L1). However, not every exchange interaction that is known to occur in spin glasses can occur in SMSC's because of some of its properties which will be discussed now.

The direct exchange, which depends on the overlap of the wave functions of the magnetic ions, is one that can be ruled out, because the spacing of the magnetic cations in alloys is too large to allow any significant overlap. In fact, tellurium anions always lie between cations and act as a screen.

Thus, some type of indirect exchange must be considered. One such indirect exchange is the RKKY (Ruderman-Kittel-Kasuya-Yosida) exchange, which represents an indirect coupling of the spins via the conduction electrons. This interaction oscillates between decaying positive and negative values as the distance between nearest neighbours increases (82F1). However, because of the low carrier concentration in these SMSC's, its contribution is negligible compared to other mechanisms.

Another indirect exchange mechanism is superexchange. This type of superexchange occurs in MnO. In this material, the transfer of interaction between nearest neighbour Mn^{2+} ions is made via localized orbits of the oxygen anion. However, in the present SMSC's, the orbitals of the tellurium ion are delocalized and form bands. For this reason, this type of interaction can also be ruled out.

Another type of superexchange mechanism that occurs when bands are formed is the Bloembergen-Rowland mechanism (55B1). In this mechanism, a Mn^{2+}

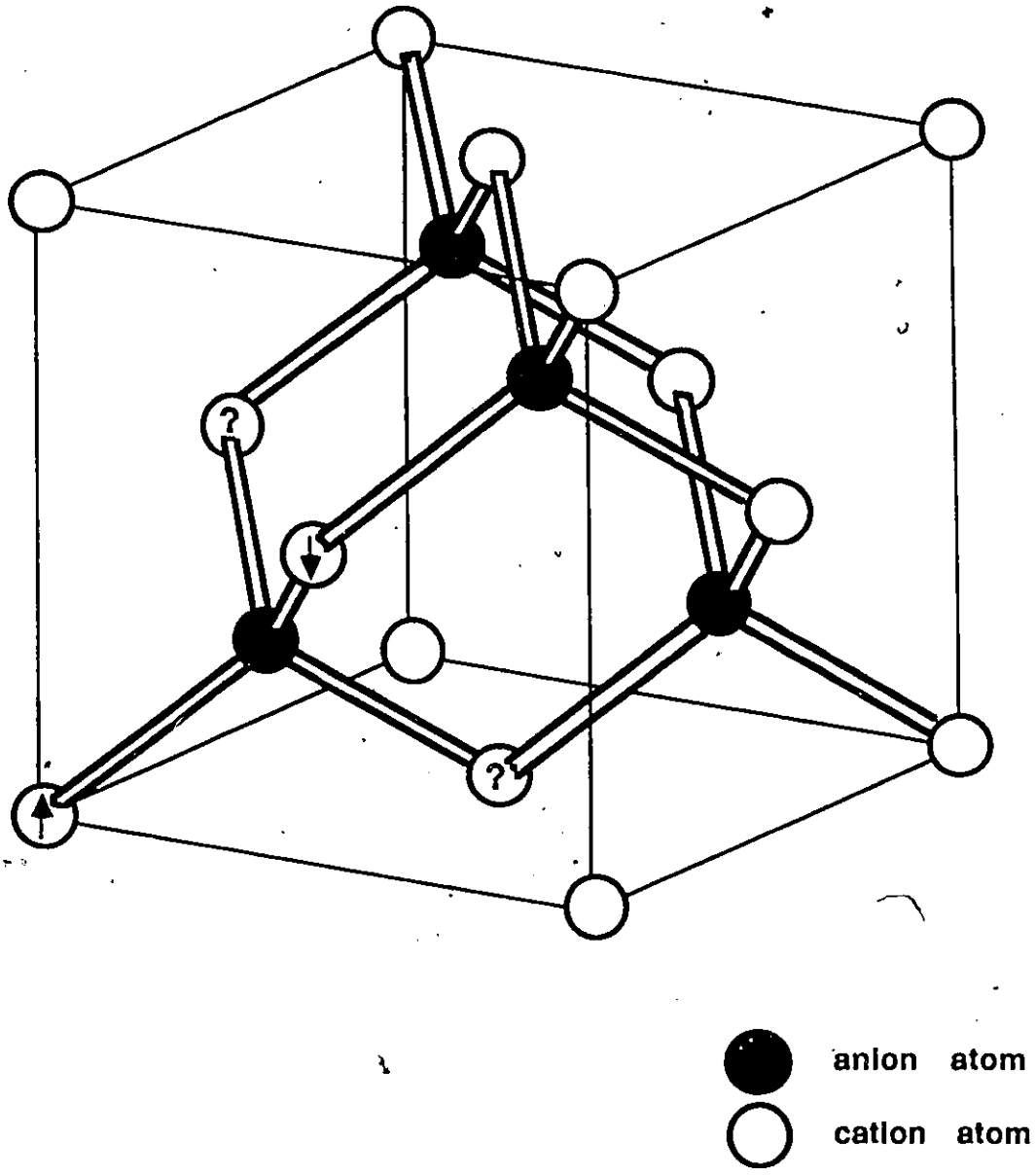

FIGURE 5.1 Frustration results in the zinc blende lattice when manganese cations are in a quandary with the direction of their spins.

ion interacts with the valence band to virtually promote an electron from the valence to the conduction band and it is this electron in the conduction band which interacts with other Mn^{2+} ions. This mechanism depends on the energy gap of the materials and since the energy gaps of the present samples are relatively wide, its contribution is expected to be at most 5% (87B1).

The indirect superexchange interaction that is known to occur in these SMSC's is that proposed by Geertsma et al. (77G1). In this mechanism, the interaction between ions takes place via a virtual transition between the valence band and the delocalized state of the manganese ion. This is the mechanism that will be analysed here.

5.3 Theory

The temperature at which a SMSC changes from a paramagnetic to a spin glass phase occurs at T_g, the spin glass transition temperature. Equating the thermal energy at that temperature with the exchange energy between two magnetic ions separated by a distance r gives (81E1, 84B1):

$$k T_g = -S (S+1) J(r) \qquad \text{(equation 5.1)}$$

where k is the Boltzman constant.

S = 5 / 2 is the spin of each manganese ion.

and J (r) is the exchange parameter.

Using the exchange parameter of the superexchange mechanism proposed by

Geertsma et al. (77G1), equation 5.1 gives:

$$k T_g = - S (S+1) I_o \frac{\exp (-\alpha r_m)}{r_m^2} \qquad \text{(equation 5.2)}$$

where $\alpha = 2 (2 m^* \varepsilon / \hbar^2)^{1/2}$ is a constant

m^* is the valence band effective mass.

ε is the difference in energy between the $3d^5$ level of Mn^{2+} with the full valence band and the $3d^6$ level of Mn^{2+} with a hole in the valence band.

$r_m = d\ z^{-1/3}$ is the mean distance between Mn cations.

$d = a / \sqrt{2}$ is the nearest neighbour cation distance.

a is the zinc blende lattice parameter.

z is the manganese concentration.

and I_o is a negative constant.

Rearranging and taking the natural logarithm of equation 5.2 gives:

$$\ln \left(\frac{a^2 T_g}{2 z^{2/3}} \right) = \ln A - \left(\frac{a}{\sqrt{2}\ z^{1/3}} \right) \alpha \qquad \text{(equation 5.3)}$$

where $A = - \frac{S (S+1) I_o}{k}$ is a constant.

Thus, a plot of $\ln (a^2 T_g / 2 z^{2/3})$ as a function of $a / \sqrt{2}\ z^{1/3}$ results in a straight line whose slope, $-\alpha$ (which depends on m^* and ε) and whose intercept, ln

A (which depends on I_o) are expected to be similar to the results of other SMSC alloy systems.

With the values of α and A derived from the graph above and with the superexchange interaction parameter J (r), values of the Curie-Weiss temperature, θ can be calculated since from the standard mean field theory (63S1):

$$\theta = \frac{2}{3} \frac{S(S+1)}{k} \sum_i n_i J_i \qquad \text{(equation 5.4)}$$

where $\sum$ represents the summation over consecutive sets of neighbours in the cation sublattice.

and n_i is the number of neighbours at a given distance.

Substituting for the superexchange parameter and replacing n_i by zn_i gives:

$$\theta = -\frac{2}{3} A z \sum_i \frac{n_i \exp(-\alpha r_i)}{r_i^2} \qquad \text{(equation 5.5)}$$

where $A = -\frac{S(S+1) I_o}{k}$ is a constant.

and r_i is the distance between cations.

Using the values of n_i and r_i calculated out to the seventh nearest neighbours (table 5.1), values of θ are calculated and compared to experimentally determined values.

Table 5.1 Values of n_i and r_i for the zinc blende structure (86W1)

n_i	r_i
12	$a/\sqrt{2}$
6	a
24	$\sqrt{3/2}\,a$
12	$\sqrt{2}\,a$
24	$\sqrt{5/2}\,a$
8	$\sqrt{3}\,a$
48	$\sqrt{7/2}\,a$

5.4 Experiment

The measurement of susceptibility was performed using the equipment of Dr. G. Lamarche. A brief description of the equipment is given by Doug Beckett (86B1). A schematic diagram is given in figure 5.2. It consists of a variable-temperature cryostat into which a moveable sample holder is inserted. Surrounding this is a cryostat kept at liquid helium temperature. This outer cryostat contains a superconducting niobium cylinder to trap magnetic fields of known strength, and two superconducting coils wound in opposite directions. These coils are connected to a SQUID (Superconducting Quantum Interference Device).

The sample holder is lowered at a slow speed through the two coils. This results in current changes in the coils to counteract the flux change arising from the magnetization of the sample. These currents are amplified through the SQUID, and the output voltage fed into a computer. The computer averages the values for an upward and then downward pass of the sample holder, converts the voltage into units of susceptibility and stores the results along with the temperature reading.

The spin-glass transition temperature, T_g is determined from d.c. magnetic susceptibility measurements in the range 4 - 250 K. This transition temperature appears as a cusp in a somewhat smooth curve of susceptibility, χ as a function of temperature, see figure 5.3. However, for some samples, the cusp is blurred out and is not too evident. Consequently, the susceptibility measurements are made on samples that are: i) cooled in and ii) cooled out of the magnetic field because the values obtained from field cooled and zero-field cooled are different at temperatures below T_g and converge at T_g, see figure 5.4.

The Curie-Weiss temperature, θ is determined experimentally by plotting the inverse of the magnetic susceptibility as a function of temperature. At high

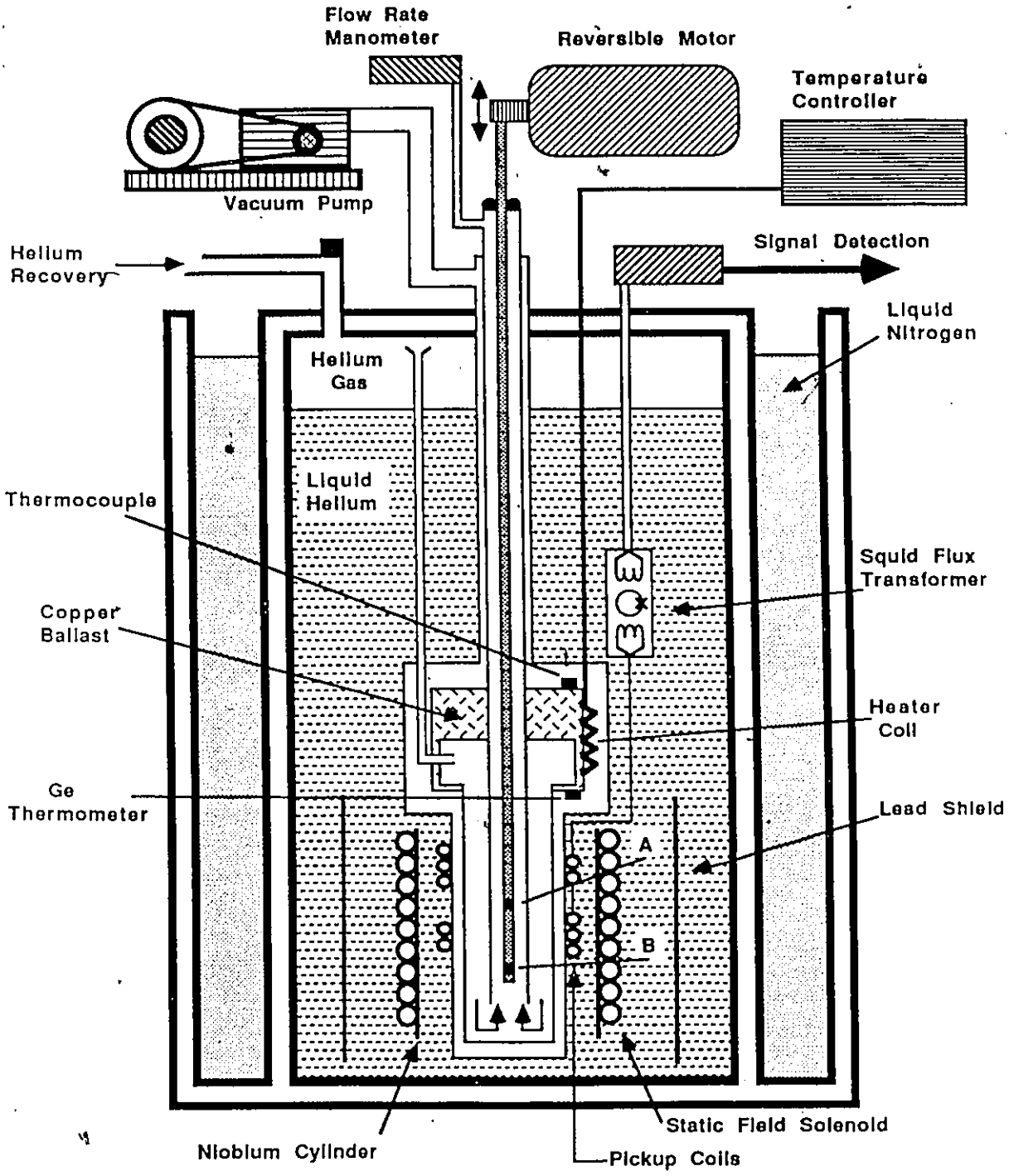

FIGURE 5.2 Schematic diagram of the magnetic susceptibility apparatus. Samples are placed in positions A and B.

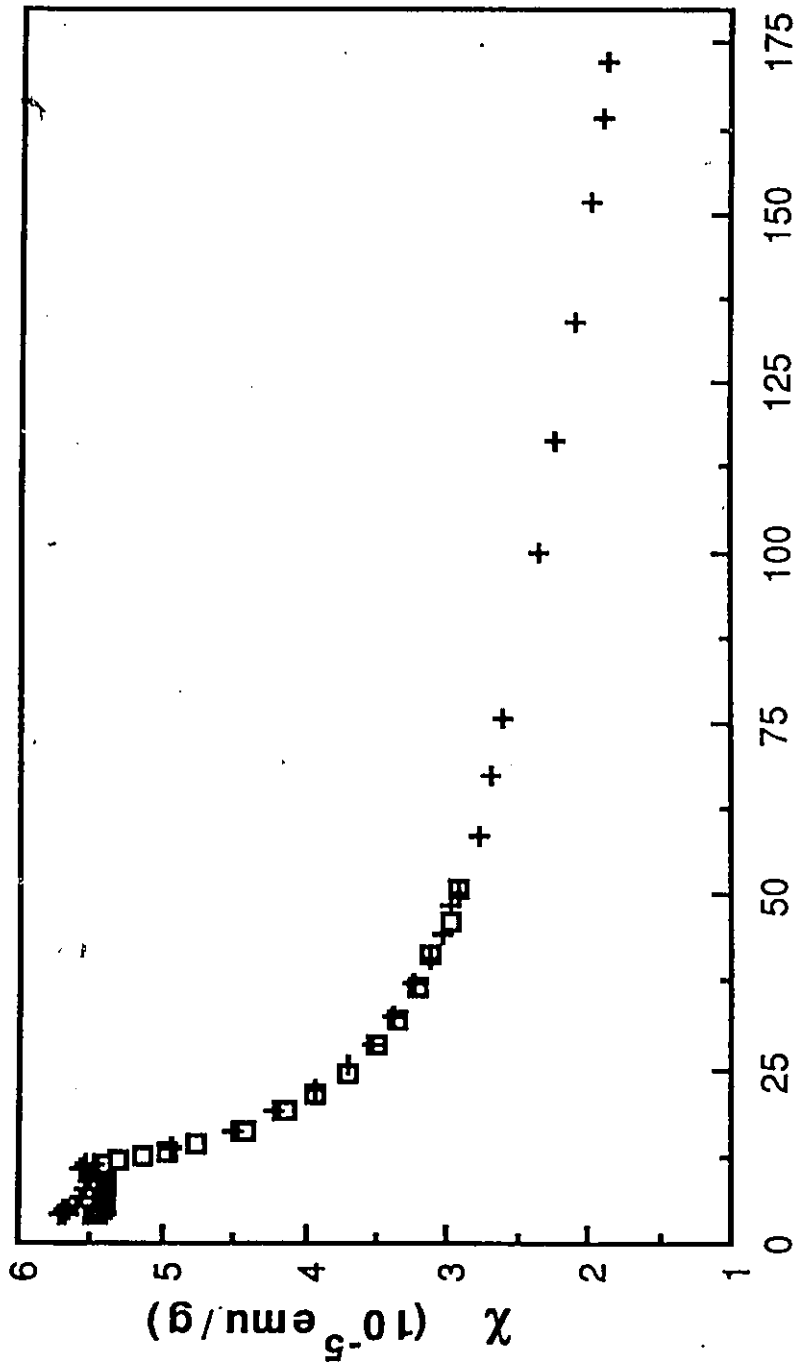

FIGURE 5.3 Variation of magnetic susceptibility with temperature for the sample 35/35/30.

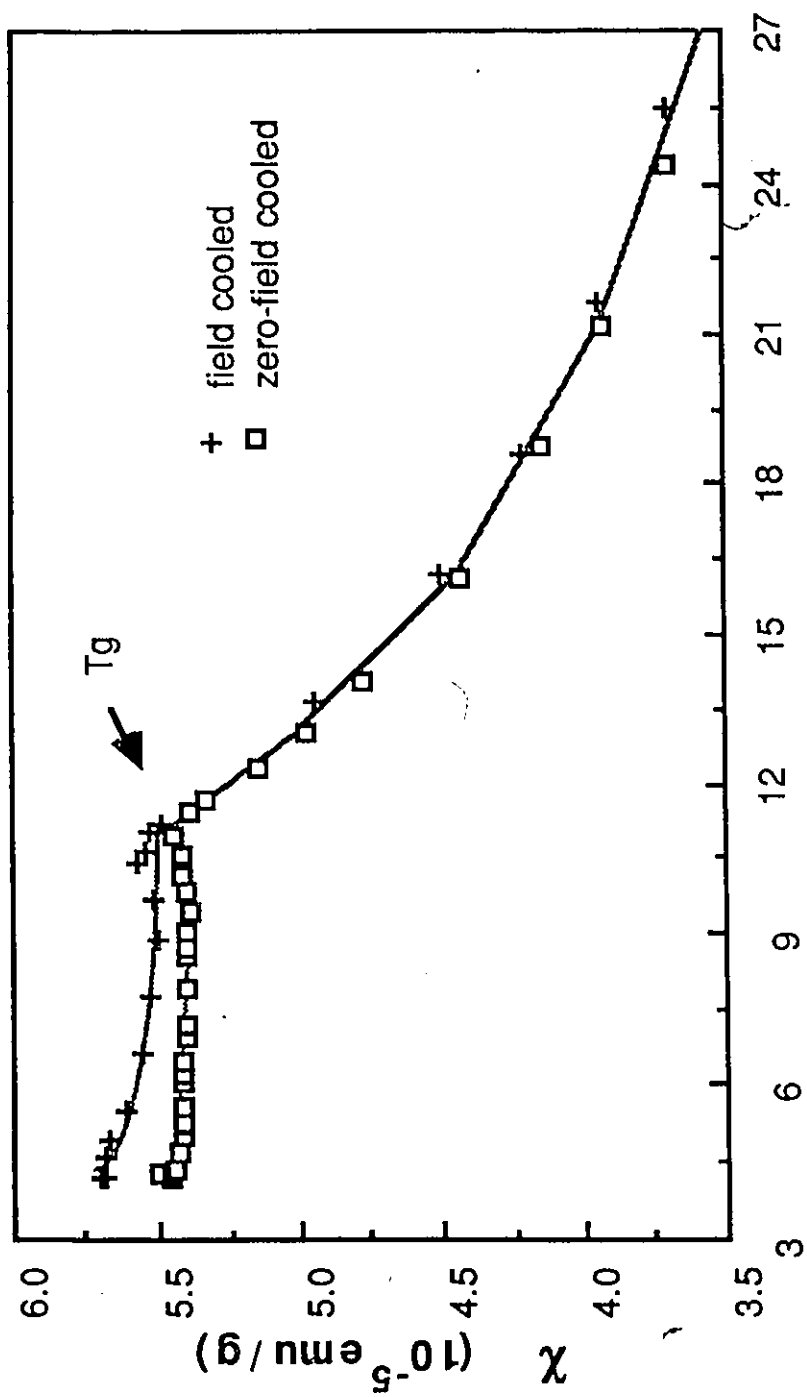

FIGURE 5.4 Variation of magnetic susceptibility with temperature for the sample 35/35/30. The spin glass transition temperature is given by the intersection of the field cooled and the zero-field cooled lines.

temperatures, the samples behave paramagnetically and according to the Curie-Weiss law (60M1):

$$\chi = \frac{C}{T - \theta} \qquad \text{(equation 5.6)}$$

or, taking the inverse, equation 5.6 gives:

$$\frac{1}{\chi} = \frac{1}{C}(T - \theta) \qquad \text{(equation 5.7)}$$

Thus, an extrapolation to the temperature axis should give experimental values of the Curie-Weiss temperature. A typical graph of $1/\chi$ as a function of temperature is shown in figure 5.5 for the sample 35/35/30.

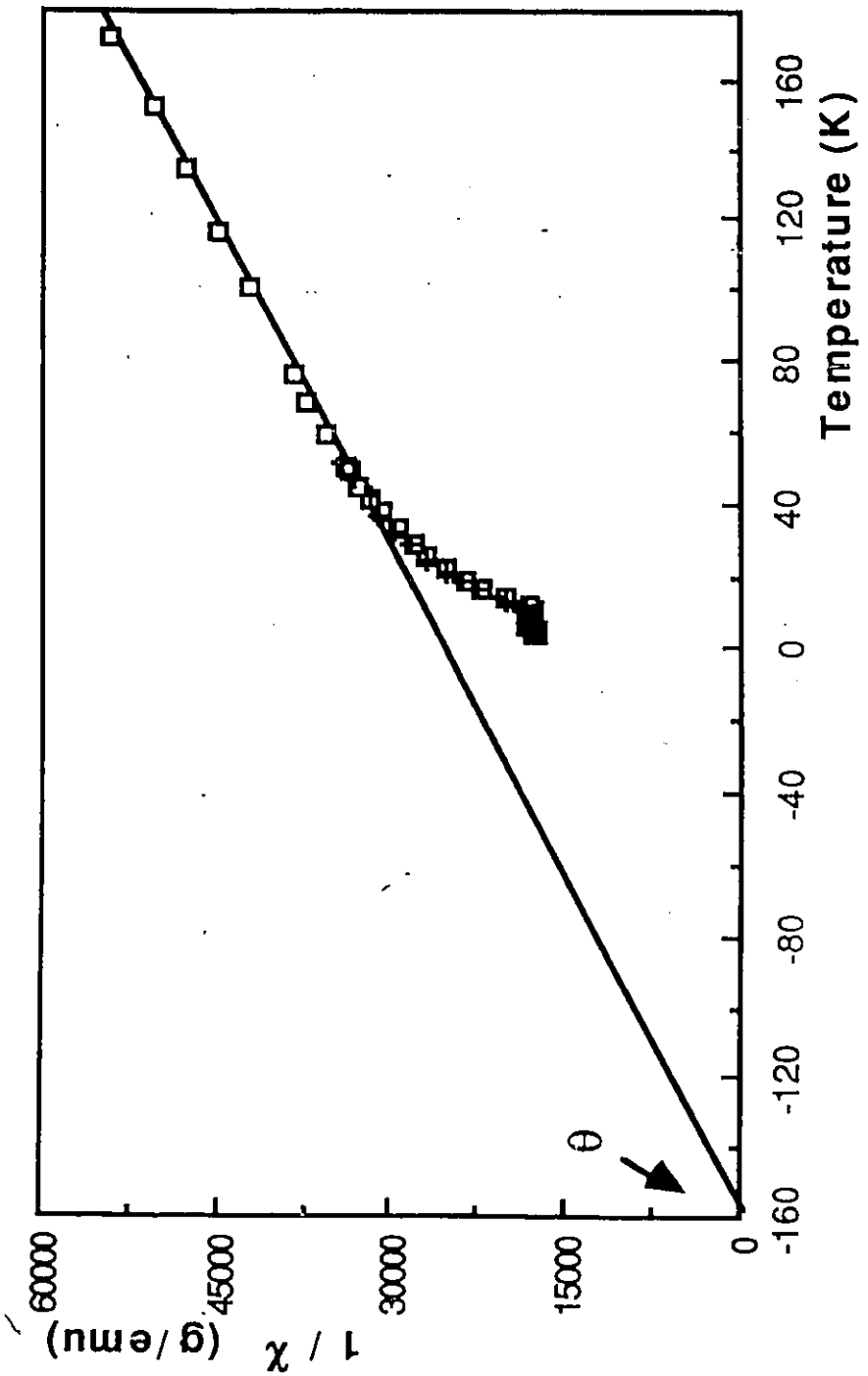

FIGURE 5.5 Variation of the inverse of magnetic susceptibility with temperature for the sample 35/35/30. The linear extrapolation at high temperatures gives the Curie-Weiss temperature.

5.5 Results and Discussion

Figure 5.6 shows the variation of the spin glass transition temperature as a function of manganese concentration. A line drawn through the theoretical nearest neighbour percolation limit of 0.196 for the fcc lattice structure (79G2) suggests that next nearest neighbour interactions are significant for $z < 0.30$. The percolation limit defines the concentration below which the system cannot sustain any freezing process that arises from nearest neighbour interaction.

Note that in figure 5.6, all the data is taken from samples of the zinc blende structure because not enough information was obtained from the chalcopyrite samples. Hence, no chalcopyrite comparison can be made with other systems, although Munkid Al-Najjar of the same semiconductor group did obtain a different slope for chalcopyrite samples (87A1).

Also, others obtained two T_g values in the susceptibility measurements of similar systems (87A1, 87N1), although only one was observed in this system. It is thought that this is due to varying degrees of ordered material and disordered material in the sample, which may be controlled by the annealing treatment. However, only one cusp was observed in susceptibility measurements of the samples of this system and the phase thought to be responsible for this is the ordered zinc blende phase. The reason for this is that the slope of the Tg versus manganese concentration graph in the $Cd_xZn_yMn_zTe$ alloy system (86D1) which crystallizes in the disordered zinc blende structure was different. This indicates that a different zinc blende structure is present. ie. ordered zinc blende. Similar results were obtained in $Cd_{2x}(AgGa)_yMn_{2z}Te_2$ (87A1) and in $Zn_{2x}(CuIn)_yMn_{2z}Te_2$ (87N1).

Figure 5.7 shows the variation of the experimental Curie-Weiss temperature, θ as a function of temperature. Because all the values of θ were negative, this

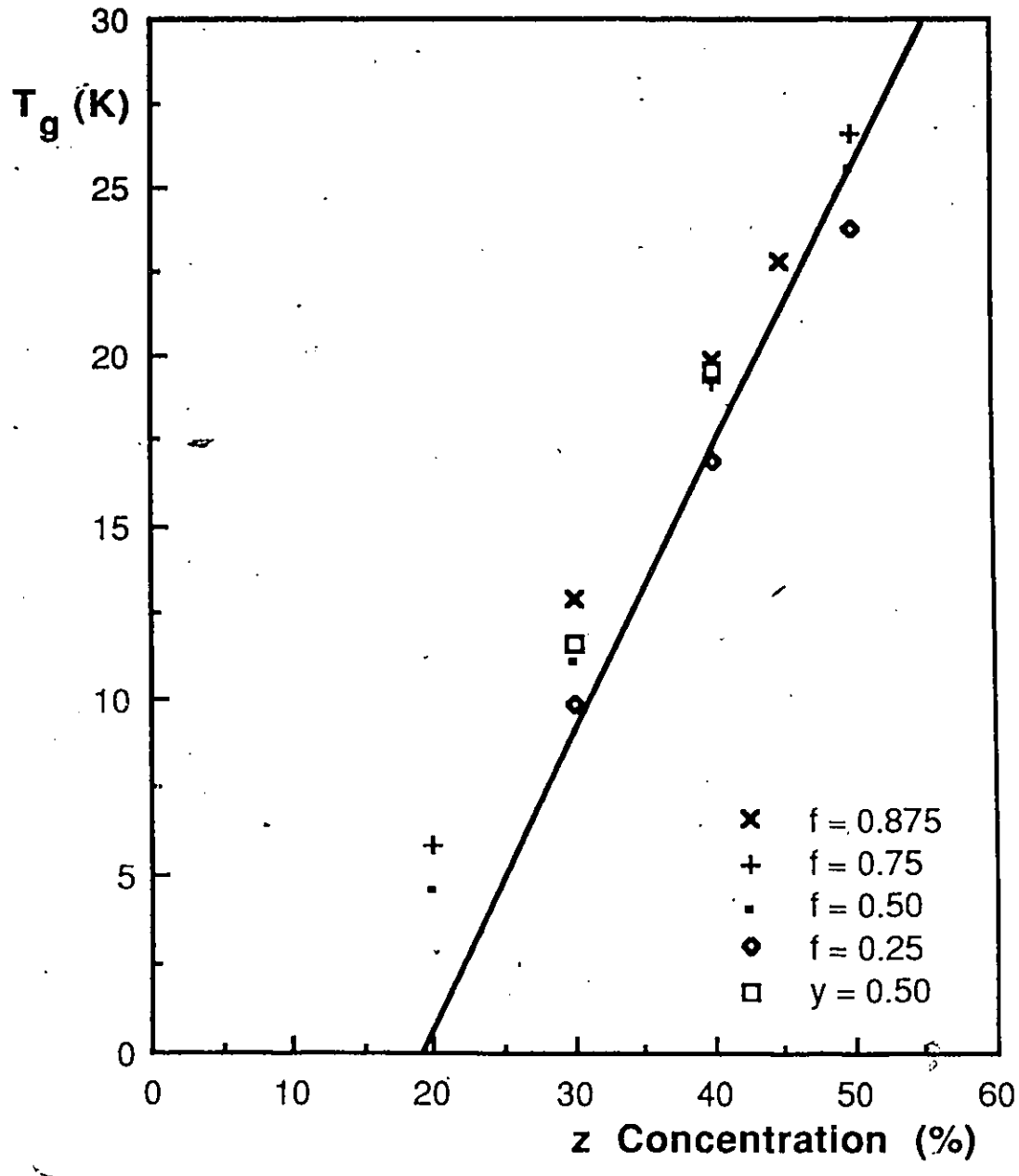

FIGURE 5.6 Variation of spin glass transition temperature with z concentration. The line was drawn to go through the known nearest neighbour percolation limit of z=19.6.

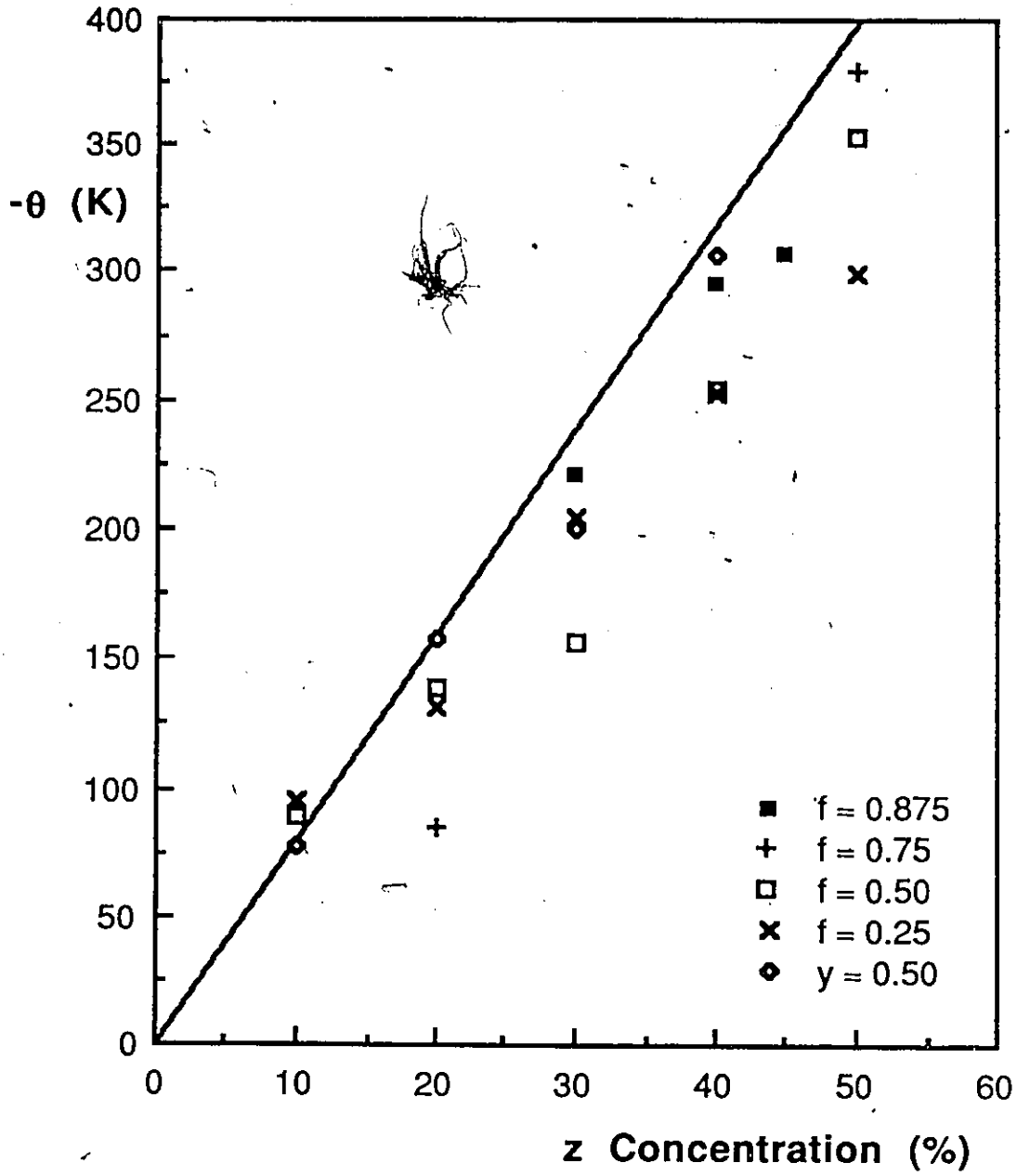

FIGURE 5.7 Variation of the Curie-Weiss temperature as a function of z concentration. The line represents the variation of the Curie-Weiss temperature which was calculated from the mean field theory using equation 5.5.

implies that an antiferromagnetic type of coupling between the spins dominates in these SMSC's.

The line in figure 5.7 represents the contribution to θ due to the superexchange mechanism, equation 5.5. This line agrees fairly well with the experimental values of θ, but it should be born in mind that if two phases are present in the sample, ie. an ordered and a disordered mixture, then the θ value observed is essentially a weighted mean of the separate θ values. Thus, this may provide a way to determine the proportion of the ordered zinc blende phase in the disordered zinc blende material.

From the plot of $\ln (a^2 T_g / 2 z^{2/3})$ as a function of $(a / \sqrt{2}\, z^{1/3})$ in figure 5.8, the values of α and A may be determined experimentally from the slope and the intercept, respectively, see equation 5.3. The values obtained in this case for the ordered zinc blende phase are $A = (150 \pm 15)$ K nm^2 and $\alpha = (5.2 \pm 0.2)$ nm^{-1}. These results may be compared with the results obtained from other similar systems. In $Cd_{2x}(AgGa)_yMn_{2z}Te_2$, Munkid Al-Najjar obtained $A = 128$ K nm^2 and $\alpha = 4.489$ nm^{-1} (87A1). Although no error estimates were given, the present results for the ordered zinc blende structure for the $Cd_{2x}(CuGa)_yMn_{2z}Te_2$ system are consistent with his.

The values of A and α were also obtained for the disordered zinc blende samples in $Cd_xZn_yMn_zTe + Cd_{1-z}Mn_zTe_{1-y}Se_y$ (86W1) and in $Cd_xHg_yMn_zTe$ (87M1). The respective values obtained for those systems are $A = (203 \pm 50)$ K nm^2 and $\alpha = (6.1 \pm 0.4)$ nm^{-1}, and $A = 232$ K nm^2 and $\alpha = 6.18$ nm^{-1}.

Thus, the values of A (which depends on I_o) and α (which depends on m* and ε) obtained are found to depend on the crystal structure involved.

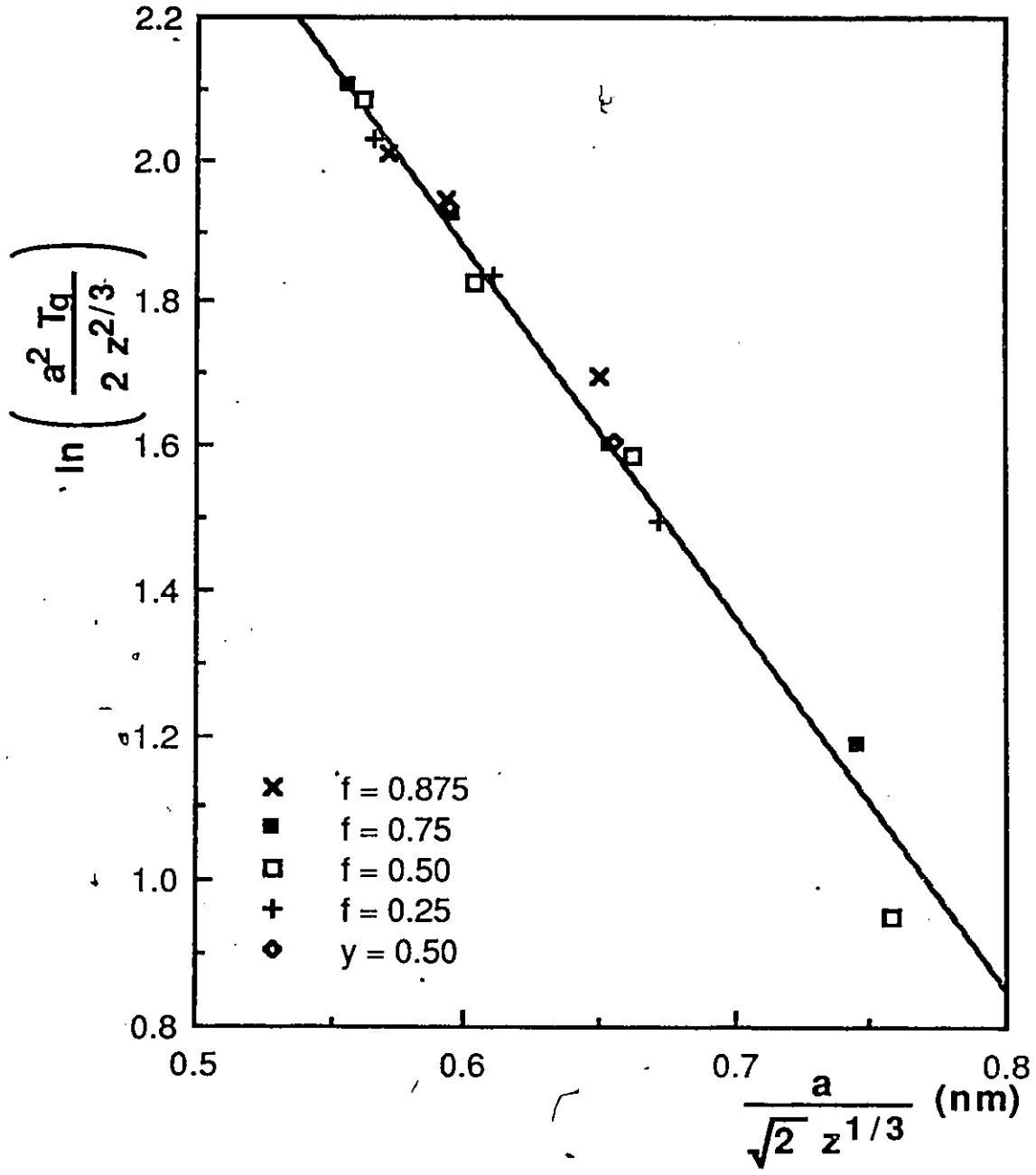

FIGURE 5.8 Fit of experimental data to equation 5.3.

CONCLUSION

In this report, crystallographic, optical and magnetic properties of the $Cd_{2x}(CuGa)_yMn_{2z}Te_2$ (x+y+z=1) alloy system have been presented.

From the crystallographic analysis, the samples were found to crystallize in two structures: a face-centered cubic zinc blende structure and a body-centered tetragonal chalcopyrite structure. However, not all the samples that were prepared could be analysed due to a lack of knowledge of the appropriate annealing temperatures which prevented equilibrium conditions from being achieved. It is suggested that additional DTA measurements on all samples of the system could provide this information.

From room-temperature measurements of optical absorption, energy gap values were obtained for single phase samples. From these values, the boundaries of the ordered and disordered phases could be obtained. However, due to the insensivity of the x-ray measurements to the presence of order and disorder in a sample, the nature of this type of ordering could not be determined. It is suggested that neutron diffraction measurements could determine the type of ordering on a similar system $Zn_{2x}(CuIn)_yMn_{2z}Te_2$ because it does not contain cadmium.

From ESR measurements, two absorption lines were observed. The broader linewidth, ΔH was due to a disordered phase and was analysed in terms of a relation derived by Chehab et al. (86C1) and by Woolley et al. (87W2). The other linewidth, ΔH_0 was thought to be due to an ordered phase.

From measurements of low-field magnetic susceptibility in the temperature range 4.2 - 250 K, values of T_g, the spin-glass transition temperature and θ, the Curie-Weiss temperature were obtained. Values of T_g and lattice parameter were

analysed for the ordered zinc blende samples in terms of the indirect superexchange mechanism of the form $J(r) = I_o\, r^{-2} \exp(-\alpha r)$ proposed by Geertsma et al. (77G1). From that analysis, the values of I_o (or A) and α obtained were found to agree with those obtained for other ordered zinc blende alloys (87A1). It was concluded that the values of I_o and α obtained were dependent on the structure involved.

Values of the Curie-Weiss θ for each sample were also calculated from the values of I_o and α, and these were shown to agree with the values determined from magnetic susceptibility measurements.

REFERENCES

45N1 Nelson, J.B. and Riley, D.P., Proc. Phys. Soc., 57, 160 (1945)

55B1 Bloembergen, N., and Rowland T.J., Phys. Rev., 97, 1679 (1955)

63S1 Smart, J.S., Magnetism, editors Rado and Suhl, Academic Press, III, 63 (1963)

66W1 Woolley, J.C. and Williams, E.W., J. Electrochem. Soc., 113 , 849 (1966)

68G1 Greenaway D.L. and Harbeke G., Optical Properties of Semiconductors, Pergamon Press, N.Y. (1968)

72W1 Wertz, J.E. and Bolton, J.R., Electron Spin Resonance: Elementary Theory and Practical Applications, McGraw-Hill Book Company, 308 (1972)

77G1 Geertsma, W., Haas, C., Sawatzky, G.A. and Vertogen, G., Physica B, 86-88, 1039 (1977)

79P1 Pamplin, B., Kiyosawa, T. and Masumoto, K., Prog. Cryst. Growth and Charact., 1, 331 (1979)

79G1 Galazka, R.R., Physics of Semiconductors 1978, Conference Series no.23 (Institute of Physics, London, 1979) p.133

79G2 Grest, G.S., Gable, E.G., Phys. Rev. Lett., 43 , 1182 (1979)

80H1 Hughes, O.H., Woolley, J.C., Lopez-Rivera, S.A. and Pamplin, B.R., Solid State Commun. 35, 573 (1980)

80L1 Lewiner, C., Gaj, J.A. and Bastard, G., J. de Physique, 41, C5-289 (1980)

81E1 Escorne, M., Mauger, A., Triboulet, R. and Tholence, J.L., Physica B, 107, 309 (1981)

81T1 Triboulet, R., and Didier, G., J. Crystal Growth, 52, 614 (1981)

82F1 Ford, P.I., Contemp. Phys., 23, 141 (1982)

82G1 Goodchild, R.G., Hughes, O.H., Lopez-Rivera, S.A., and Woolley, J.C.,

Can. J. Phys., 60, 1096 (1982)

82G2 Galazka, R.R., Lect. Notes Phys., 152, 294 (1982)

83B1 Brun del Re, R., Donofrio, T., Avon, J.E., Majid, J., and Woolley, J.C., IL Nuovo Cimento, 2D, 1911 (1983)

83H1 Higgins, R.J., Electronics with Digital and Analog Integrated Circuits, Prentice-Hall, 501 (1983)

84B1 Brandt, N.B. and Moschalkov, V.V., Adv. Phys., 33, 193 (1984)

84W1 Webb, D.J. Bhagat, S.M. and Furdyna, J.K., J. Appl. Phys., 55, 2310 (1984)

85C1 Chehab, S.F., and Woolley, J.C., J. Less-Common Metals, 106, 13, (1985)

85Q1 Quintero, M., Ph.D. Thesis, University of Ottawa, p.37 (1985)

85Q2 Quintero, M., Ph.D. Thesis, University of Ottawa, p.38-40 (1985)

85Q3 Quintero, M. and Woolley, J.C., Phys. Stat. Sol. A, 92, 449 (1985)

85S1 Sayad, H.A. and Bhagat, S.M., Phys. Rev. B, 31, 591 (1985)

85Y1 Yoodee, K., Ph. D. Thesis, University of Ottawa , p.14-16 (1985)

86B1 Beckett, D., Master's Thesis, University of Ottawa (1986)

86C1 Chehab, S., Lamarche, G., Manoogian, A. and Woolley, J.C., J. Mag. Mag. Mat., 59, 105 (1986)

86D1 Donofrio, T., Ph. D. Thesis, University of Ottawa (1986)

86Q1 Quintero, M., Dierker, L. and Woolley, J.C., J. of Solid State Chem., 63, 110 (1986)

86W1 Woolley, J.C., Chehab, S.F., Donofrio, T., Manhas, S., Lamarche, G. and Manoogian, A., J. Mag. Mag. Mat., 61, 13 (1986)

87A1 Al-Najjar, M., Master's Thesis, University of Ottawa (1987)

87B1 Beckett, D.J.S., Chehab, S.F., Lamarche, G. and Woolley, J.C., in press

87M1 Manhas, S., Khulbe, K.C., Beckett, D.J.S., Lamarche, G. and Woolley,

J.C., in press

87N1 Neal, C., Master's Thesis, University of Ottawa (1987)

87Q1 Quintero, M., Grima, P., Tovar, R., Goudreault, R., Bissonnette, D. and Woolley, J.C., to be published

87W1 Woolley, J.C., Lamarche, G., Manoogian, A., Quintero, M., Dierker, L., Al-Najjar, M., Proulx, D., Neal, C., and Goudreault, R., Proceedings of the 7th International Conference on the Ternary and Multiternary Compounds, Mat. Research Society, 479 (1987)

87W2 Woolley, J.C., Chehab, J.F., Donofrio, T., Manhas, S., Manoogian, A. and Lamarche G., J. Mag. Mag. Mat., 66, 23 (1987)